

# Topographic Effects on Internal Waves at Barkley Canyon

Kurtis Anstey

V00939802

Department of Physics and Astronomy

University of Victoria

November 10, 2021

Dr. Jody Klymak (University of Victoria)

Dr. Steven Mihaly (Ocean Networks Canada)

Dr. Richard Thomson (Institute of Ocean Sciences)

## Table of Contents

<b>List of Figures</b>	<b>3</b>
<b>1 Abstract</b>	<b>4</b>
<b>2 Introduction</b>	<b>5</b>
<b>3 Theory</b>	<b>7</b>
<b>4 Data</b>	<b>11</b>
<b>5 Methods</b>	<b>14</b>
<b>6 Results</b>	<b>15</b>
6.1 Observations . . . . .	15
6.1.1 Mean currents . . . . .	15
6.1.2 High-pass currents . . . . .	17
6.2 Depth dependence . . . . .	20
6.3 Frequency dependence and seasonality . . . . .	23
6.3.1 Sub-diurnal and diurnal . . . . .	23
6.3.2 Near-inertial . . . . .	26
6.3.3 Semidiurnal . . . . .	29
6.3.4 Continuum . . . . .	32
<b>7 Discussion</b>	<b>37</b>
7.1 Axis mean currents . . . . .	37
7.2 Tidal forcing . . . . .	37
7.3 Near-inertial forcing . . . . .	43
7.4 Continuum analysis . . . . .	49
<b>8 Summary and conclusions</b>	<b>56</b>
<b>9 Appendix A: Supplemental plots</b>	<b>58</b>
9.1 Wind comparisons . . . . .	58
9.2 Continuum correlations . . . . .	58
<b>10 References</b>	<b>63</b>

## List of Figures

1	IW processes . . . . .	6
2	IW in a two-layer system . . . . .	8
3	IW and topography . . . . .	9
4	Barkley Canyon site map and semidiurnal criticality . . . . .	10
5	ADCP frequency, deployment, and data availability . . . . .	11
6	Site topography . . . . .	12
7	Averaged stratification and WKB scaling factor . . . . .	13
8	Low-pass velocities . . . . .	16
9	High-pass velocities - April 2013 . . . . .	18
10	PSD and rotary spectra . . . . .	19
11	Depth-frequency - Slope . . . . .	21
12	Depth-frequency - Axis . . . . .	22
13	Depth-band spectra - Sub-diurnal - Slope . . . . .	24
14	Depth-band spectra - Sub-diurnal - Axis . . . . .	25
15	Depth-band spectra - Diurnal - Slope . . . . .	27
16	Depth-band spectra - Diurnal - Axis . . . . .	28
17	Depth-band spectra - Near-inertial - Slope . . . . .	30
18	Depth-band spectra - Near-inertial - Axis . . . . .	31
19	Depth-band spectra - Semidiurnal - Slope . . . . .	33
20	Depth-band spectra - Semidiurnal - Axis . . . . .	34
21	Depth-band spectra - Continuum - Slope . . . . .	35
22	Depth-band spectra - Continuum - Axis . . . . .	36
23	Axis along-canyon mean-flow . . . . .	38
24	Diurnal spring-neap forcing . . . . .	39
25	Semidiurnal spring-neap forcing . . . . .	41
26	NI slab response - 2013 . . . . .	44
27	NI correlations . . . . .	45
28	NI vertical modes . . . . .	46
29	High-frequency resolution PSD - 2013 . . . . .	47
30	Continuum $a$ and $b$ fIT . . . . .	49
31	Continuum / GM ratios . . . . .	51
32	Dissipation and diffusivity . . . . .	53
33	Continuum forcing - Slope . . . . .	54
34	Continuum forcing - Axis . . . . .	55

## 1 Abstract

We make use of four overlapping years of ADCP horizontal velocity time-series data near Barkley Canyon, from both slope and canyon sites, to examine the effects of variable topography on the local currents and internal wave field. Results indicate there is consistent up-canyon mean-flow above a near-bottom down-canyon layer. There is little inter-annual variability. There is frequency dependent focusing of spectral power near topography, up to  $1.5 \times$  orders of magnitude 150 m above the continental slope, and up to  $2 \times$  orders of magnitude 250 m above the canyon bottom, with unique seasonality for individual constituents. There is little inter-annual variability outside of sub-diurnal and near-inertial seasonality. Sub-diurnal and diurnal flows are sub-inertially trapped along topography, and the diurnal band appears to be forced locally (barotropically). Free semidiurnal internal tides are focused and reflected near critical topography, and appear to experience both local and remote (baroclinic) forcing. The near-inertial band is attenuated near the slope, yet enhanced near the canyon bottom, with intermittent forcing that appears linked to regional wind events, high-mode propagation, and the seasonal mixed-layer depth. A near-topography enhanced internal wave continuum (up to  $7 \times$  GM) indicates increased rates of dissipation (exceeding  $10^{-8}$  W/kg) and diffusivity (exceeding  $10^{-4}$  m<sup>2</sup>/s), with seasonality correlations suggesting a cascade of energy from low-frequency constituents (primarily semidiurnal, with contributions from the sub-diurnal on the slope, and near-inertial in the canyon) to high-frequency dissipative processes.

## 2 Introduction

Internal waves (IW) are slow-moving, low-frequency, sub-surface gravity waves that exist within density gradients in the ocean interior (Garrett & Munk, 1979). They have wavelengths up to kilometres long, and oscillate in a range between the local Coriolis (inertial,  $f$ ) and Brunt–Väisälä (buoyancy,  $N$ ) frequencies (Garrett & Munk, 1979). They are forced by weather - as near-inertial (NI) IW are generated by surface winds exciting currents in the mixed layer that 'pump' energy into the IW field, below (Garratt, 1977) - or by tides and currents moving over irregular seafloor topography, generating baroclinic waves that can propagate through the stratified ocean (Hendershott & Garrett, 2018). Nonlinear interactions with irregular topography can cause incident IW to scatter, reflect, or focus and break, leading to mixing (Martini et al., 2013).

As the wind and tides are ever-present, IW are prevalent ocean phenomena. As early as the mid-19th century, scientists such as Stokes and Rayleigh were investigating properties of fluid density and stratification, essential for IW propagation (Garrett & Munk, 1979). IW were mistaken as consistent noise in early 20th-century hydrocast readings, and Ekman discussed their effects in his seminal theories on fluid mechanics (Garrett & Munk, 1979). In the late-20th century, Garrett and Munk (1979) developed the canonical Garrett-Munk (GM) spectrum defining the characteristic frequency and wavenumber continuum of open-ocean IW, to better understand their role in ocean processes. As instrumentation improved, scientists continued to uncover the contributions of IW to both small- and large-scale physical systems, such as mixing and the overturning circulation (Figure 1; Garrett & Munk, 1979). Recent studies have focused on IW generation and dissipation (Terker et al., 2014; Kunze, 2017), tidal and wind forcing and seasonal variability (Alford et al., 2012; Thomson & Krassovski, 2015), and enhanced mixing due to IW interactions with irregular topography (Nash et al., 2004; Kunze et al., 2012; Gemmrich & Klymak, 2015).

As IW and internal tides (IT) approach seamounts, slopes, or canyons, their energy is focused and can cascade from low- to high-frequency processes, eventually dissipating as heat (Garrett & Munk, 1979). Dissipation leads to an energetic local environment, evident as turbulent processes on the fine- (1 - 100 m vertical) and micro-scales ( $< 1$  m vertical) (Garrett & Munk, 1979; Kunze et al., 2012). These processes drive regional transport of energy and momentum, and the mixing of heat, pollutants, and biological constituents (Kunze et al., 2012). Topography-forced IW mixing helps to set ocean stratification, layers that influence both small- and large-scale physical systems (Garrett & Munk, 1979). As such, knowledge of topography-IW interactions is important

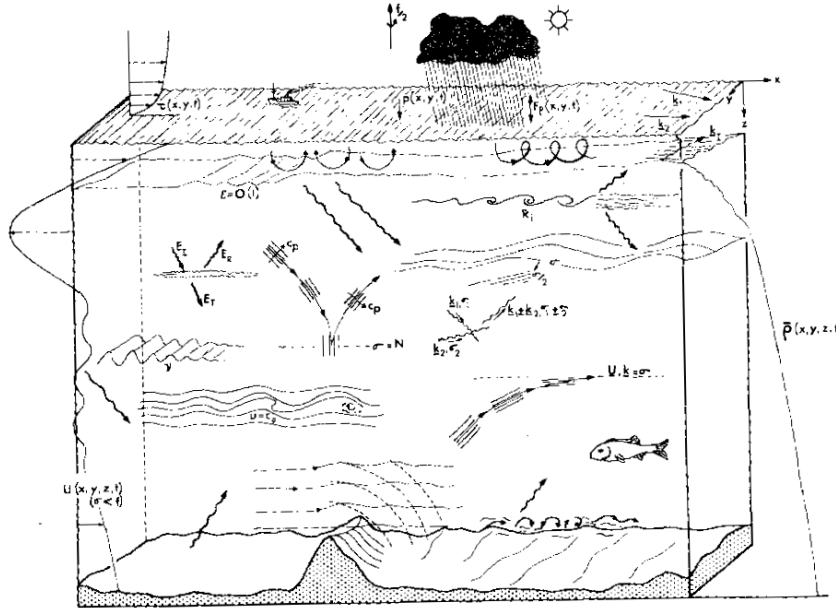


**Figure 1.** Generalised depiction of IW processes in the ocean, as envisioned by Garrett and Munk (1979). IW are forced by, coincide with, or contribute to most physical processes in the ocean.

for understanding both regional dynamics and the coupled ocean-atmosphere climate system (Garrett & Munk, 1979).

Topography focused IW studies are global, ongoing at locations such as the Hawaiian ridge (Alford et al., 2007), the continental slopes of the South China Sea (Klymak et al., 2011), and the slope-incising submarine canyons of the northeast Pacific (Allen et al., 2001; Carter & Gregg, 2002; Kunze et al., 2012; Terker et al., 2014). Canyons and their adjacent continental slopes have been identified as hot spots of IW activity, that both generate (Carter & Gregg, 2002) and dissipate (Allen et al., 2001; Kunze et al., 2002) IW and IT. At Monterey Canyon, IW and IT have been found to scatter, reflect, and focus depending on the angles of incident IW and the impacted slope (Figure 3; Kunze et al., 2012); force near-bottom turbulent layers that drive mixing (Carter & Gregg, 2002; Kunze et al., 2002); and, cause dissipation and IT generation at irregular topography (Terker et al., 2014). Further research on IW interactions with submarine canyons and their adjacent continental slopes is thought to be essential to understanding seasonal upwelling, diapycnal mixing, and cross-shelf exchange (Burrier, 2019).

In Canada, IW are regularly observed on the productive Vancouver Island Continental Shelf (VICS) (Allen et al., 2001), a relatively broad (about 80

km) shelf region with a canyon-incised continental slope. Regional IW observations have led to insight on non-linear wave-wave interactions between surface generated NI IW and upward propagating semidiurnal IT (Mihaly et al., 1998), and the presence of diurnal baroclinic shelf waves forced by tidal oscillations near the mouth of the Juan de Fuca Strait (Thomson & Crawford, 1982). Seasonally variable regional currents (Thomsons & Krassovski, 2015) have been associated with observations of vorticity stretching and upwelling at the head of the shelf-incising Barkley Canyon, suggesting considerable canyon influence on local water properties, transport of biological constituents, and overall shelf productivity (Allen et al., 2001; Juniper et al., 2013; Doya et al., 2013; Chauvet et al., 2018). However, there is a lack of topography-IW observations necessary to fully understand the slope and canyon influence on VICS physical processes. Further research into the IW field at Barkley Canyon can provide insight into regional phenomena such as the high productivity of the VICS, as well as an additional case study for topography focused IW research, globally.

This study evaluates horizontal velocity data from two sites, one within Barkley Canyon and another on the adjacent continental slope, to characterise the interactions of IW and IT with topography, and the potential influence on local mixing. Sub-tidal, tidal, NI, and high-frequency (continuum) IW bands are evaluated for depth-dependence and seasonality, including a forcing analysis of variability due mean-currents, tides, and wind. The state of the high-frequency IW continuum is evaluated for topographic enhancement through comparison with canonical GM theory, and estimates of dissipation and diffusivity to approximate mixing. Key findings include topography guided currents, with consistent up-canyon flow above a near-bottom down-canyon layer, near-topography enhancement of IW spectral power with frequency-dependent seasonality, NI IW attenuation near the continental slope with intermittent forcing from wind events and mixed-layer depth, and a heightened continuum state with seasonality correlations suggesting a cascade of energy from low-frequency constituents to high-frequency dissipative processes.

### 3 Theory

Vertical displacements in a fluid can be classified as either barotropic, where the displacement is dependent only on pressure,  $P(z)$  (where  $z$  is depth), or as baroclinic, where the displacement is also a function of density,  $\rho(z)$ , temperature,  $T(z)$ , etc. (Figure 2). For example, the surface tides are barotropic, affecting most of the water column as the surface oscillates. IW are baroclinic, perturbations that exist along density interfaces in the stratified ocean

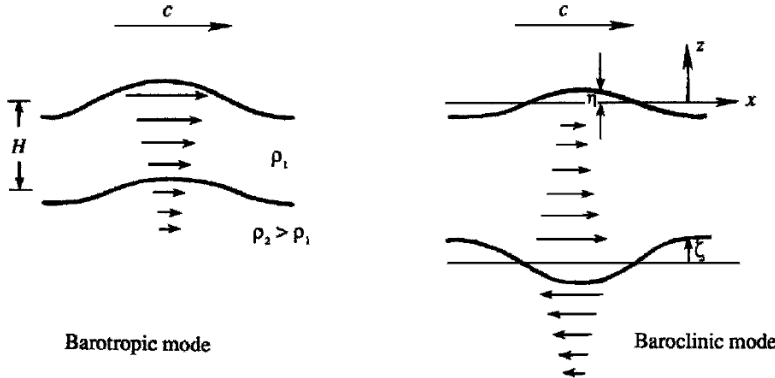


**Figure 2.** IW in a two-layer system. Graphic representation of the difference between barotropic and baroclinic flow. Adapted from Kundu & Cohen (2008).

interior. IW are highly dependent on stratification, often characterised by the depth-dependent buoyancy frequency,  $N(z)$ , defined as:

$$N^2(z) = -\frac{g}{\rho_0} \frac{d\rho}{dz} \quad (1)$$

where  $g$  is the acceleration due to gravity, and  $\rho_0$  a constant reference density. IW are commonly found in continuously stratified fluids such as the ocean interior, where they may exist both non-isotropically and rotationally, with rotation effects defined by the consistency relation:

$$\frac{CW}{CCW} = \frac{(\omega + f)^2}{(\omega - f)^2} \quad (2)$$

where the Coriolis frequency,  $f = 2\Omega\sin\phi$  ( $\Omega$  is the rotation rate of the Earth, and  $\phi$  is latitude), and  $N(z)$  are the lower and upper spectral bounds for IW frequency,  $\omega$  (Kundu and Cohen, 2008).

As IW and IT approach irregular topography (continental slopes, canyons, etc.), the angle of the incident wave energy,  $\alpha$ , and the slope of the topography,  $\beta$ , have an influential relationship on the behaviour of the interaction (Figure 3) (Lamb, 2014). The angle of propagation of an incident, free IW in a continuously stratified fluid is:

$$\alpha(z) = \sqrt{\frac{(\omega^2 - f^2)}{(N(z)^2 - \omega^2)}} \quad (3)$$

where  $\omega$  is the frequency of the incident wave (Nash et al., 2004; Garrett and Kunze, 2007; Lamb, 2014). The bathymetric slope,  $\beta = \nabla H$ , is determined

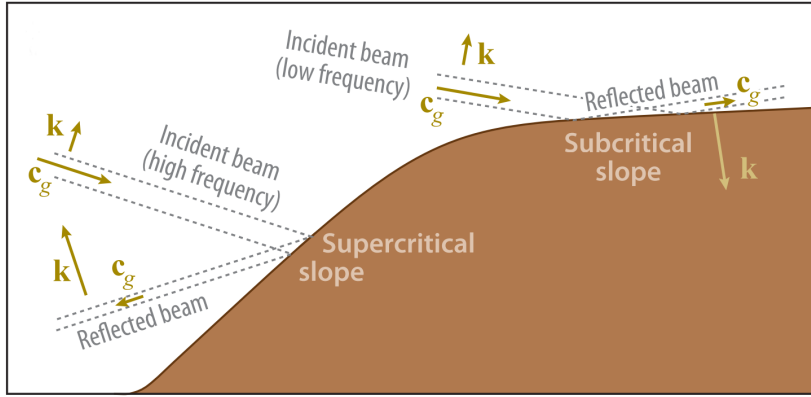


**Figure 3.** Graphic of IW interactions with slope topography (Lamb, 2014). The propagation angle of an IW depends on frequency and stratification. Depending on the slope of topography, incident IW can be scattered up, reflected down, or focused, possibly breaking.

from the gradient magnitude of the local topography, and used to determine regions of IW and IT criticality, as in Figure 4 (Martini et al., 2011). As  $\alpha$  depends on  $N(z)$ , the characteristic ray path of an IW bends with depth. If  $\beta > \alpha$  a slope is supercritical and incident wave energy is reflected downward (see Figure 6); for  $\beta \approx \alpha$  a slope is near-critical and incident wave energy is focused, potentially forcing non-linear breaking and dissipation; and, for  $\beta < \alpha$  the slope is considered subcritical and incident wave energy is scattered upward (Klymak et al., 2011). The combined effects of reflection, scattering, and focusing of IW and IT in these regions can lead to near-topography layers of increased IW energy (Lamb, 2014).

Regions near-critical to tidal frequencies are also known as hot-spots for generation of baroclinic IT, including continental slope, shelf-break, and canyon topography, though IT can be generated over non-critical irregular topography through the friction of tidal oscillations (Garrett and Kunze, 2007). Topographically generated IW and IT that are within the frequency bounds of  $f$  and  $N(z)$  radiate away baroclinically, while those not within the bounds are trapped to the local topography, dissipating locally (Kunze, 2012). Even at latitudes where the oscillating tidal frequency is sub-inertial, baroclinic 'shelf waves' can still be generated by irregular topography, trapped along the continental margin where the topographic gradient of the shelf acts as a restoring force for horizontal propagation (Crawford and Thomson, 1984; Brink, 1991).

In addition to topographically generated IW and IT, there is significant input into the oceanic IW field from wind (Alford et al., 2016). NI energy is deposited

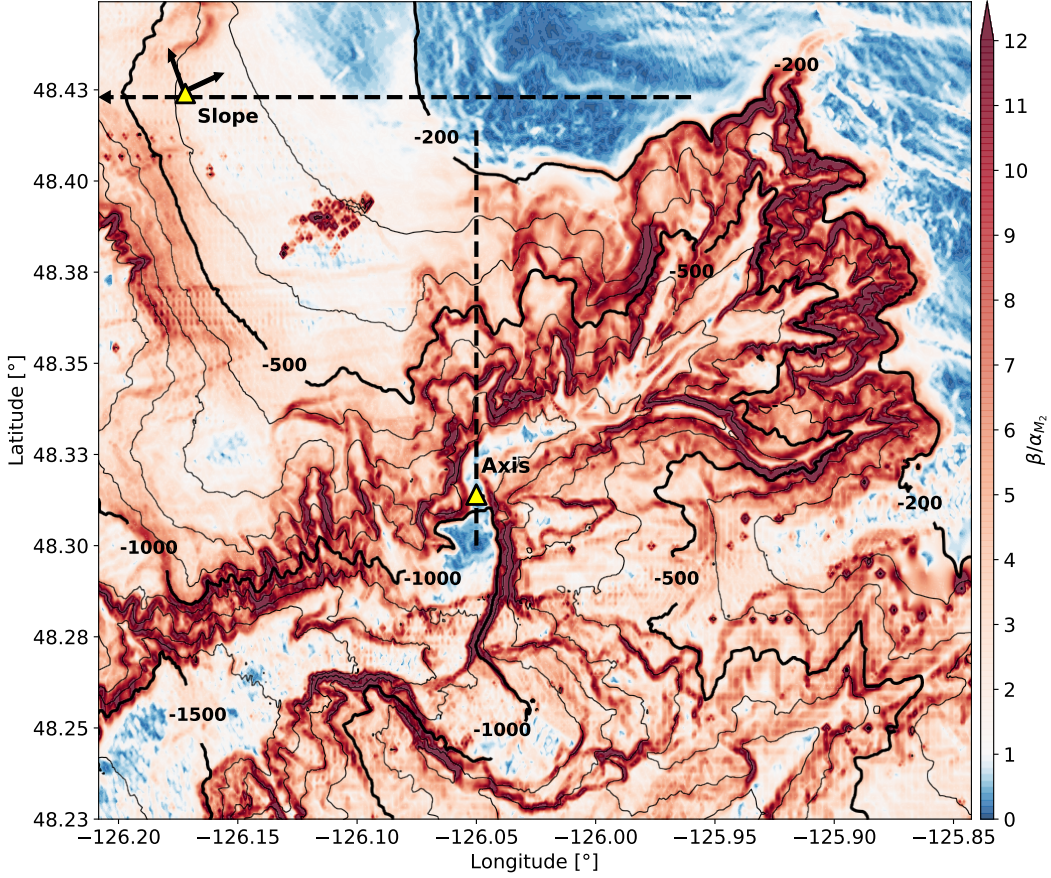


**Figure 4.** Site map and semidiurnal criticality of Barkley Canyon. Criticality is found by dividing the gradient slope ( $\beta$ ) of topography by the depth-dependent semidiurnal propagation angle ( $\alpha_{M2}$ ). Most of the region is supercritical ( $> 1$ ) to the M<sub>2</sub> IT, with notable exceptions on the shelf and canyon floor near the Axis site. Arrows at the Slope site indicate 30° rotation of velocity data to match approximate along-slope ( $v$ ) direction of mean currents; Axis data were not rotated, as the along-canyon ( $v$ ) component is aligned N-S. Dashed black lines indicate topography cross-sections used in Figure 6.

into the surface mixed-layer (ML), forcing NI currents that 'strum' IW modes, generating NI IW that propagate downward and equatorward into the ocean interior (Alford et al., 2016). For a flat-bottom basin bounded by the ocean surface, the vertical structure of the IW modes exist as solutions to the Sturm-Liouville equation (Alford and Zhao, 2007):

$$\frac{\partial^2}{\partial z^2} \eta(z) + \frac{N^2(z)}{c_n^2} \eta(z) = 0 \quad (4)$$

with boundary conditions  $\eta(0) = \eta(D) = 0$ , where  $D$  is the total water depth,  $\eta$  is surface displacement,  $n$  the mode number, and  $c_n$  the modal eigenspeed.

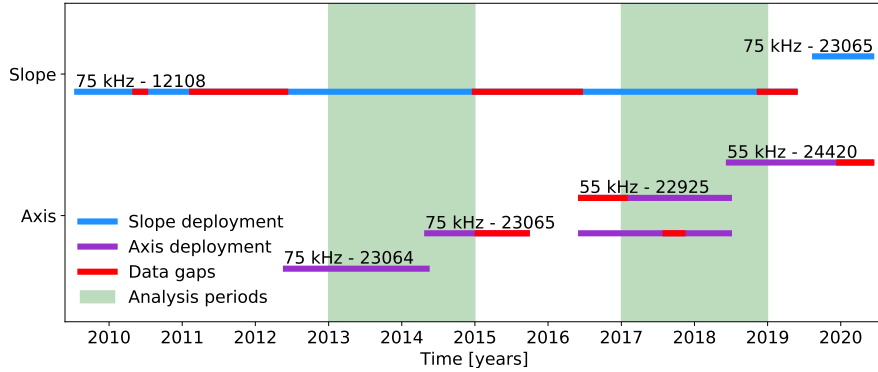


**Figure 5.** ADCP operating frequency, deployment periods, and data availability for the Slope and Axis sites. ONC operates and maintains regional instruments as part of the NEPTUNE cabled observatory. Due to maintenance and redeployment, years with comprehensive overlapping coverage (2013, 2014, 2017, and 2018) were selected for analysis.

Low-modes tend to dominate IW energy and largely propagate horizontally, while high-mode energy typically radiates downward (Alford et al., 2016). The superposition of many modes forms an IW beam (Lamb, 2014), and the combined effects of both incident and locally generated IW and IT interactions form the IW field.

## 4 Data

The Barkley Canyon velocity data is unique for both temporal and spatial considerations. Located at approximately 48.33°N 126.03°W, Barkley Canyon is about 75 km southwest of the coast of Vancouver Island, incising the continental slope and shelf (Figure 4; Barkley Canyon, 2013). Barkley Canyon is a winding canyon up to 6 km wide and 13 km long, with an adjacent shelf-break region beginning around -150 m depth (Allen, 2001). Spread across the local topography, Acoustic Doppler Current Profilers (ADCP) provide current data for Ocean Networks Canada's (ONC) NEPTUNE cabled observatory (2013). ADCP emit acoustic beams that triangulate Doppler shifts in the water column, providing directional time series through depth. The ADCP and data are operated and distributed by ONC; the Oceans 2.0 data portal offers publicly available data spanning over a decade. This is substantially lengthy dataset for IW research, allowing for typically difficult analysis of long-term variability.

Relevant ADCP were chosen at both the upper continental slope 'Upper Slope' (Slope) and the canyon-bottom Axis sites (Figure 4), 15 km apart, to allow for spatial

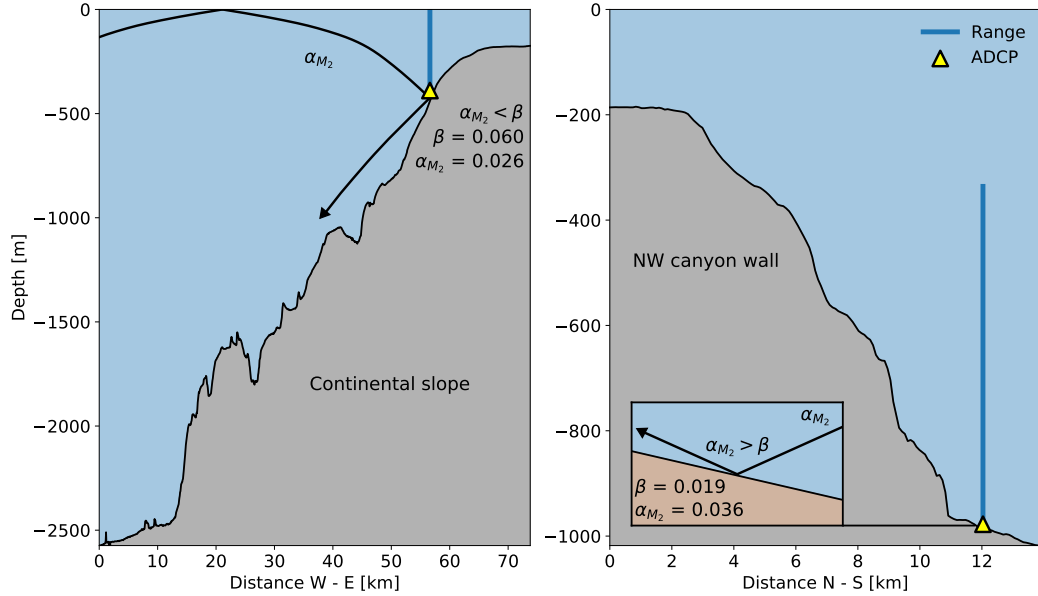


**Figure 6.** Site topography cross-sections with ray tracing. Depicted are the relative locations for Slope (left) and Axis (right) instrument moorings. Horizontal cross-sections were taken in the W-E (Slope) and N-S (Axis) directions, represented by the dashed black lines in Figure 4. Slope sIT below the VICS shelf-break while Axis is located on the floor of Barkley Canyon (right). An incident ray is shown for  $M_2$ , accounting for depth-dependent stratification, as well as local criticality at each site.  $\alpha$  is the angle of propagation, and  $\beta$  is the slope of the topography. In general, the Slope region is supercritical, while the Axis region is both subcritical (floor) and supercritical (walls).

analysis of simultaneous IW interactions at varied topography. The 75 kHz Slope instrument sIT below the VICS shelf-break at a depth of -378 metres (Figure 6), 15 km NW of Barkley Canyon. The 75 & 55 kHz Axis instruments are located at a narrow north-south channel in Barkley Canyon, about midway along IT length at a sharp bend, at a depth of -968 metres (Figure 6). The 75 kHz Teledyne RDI Workhorse Long Ranger instruments have a vertical resolution of 8 m depth bins, and a continuous sampling rate of 2 seconds. The 55 kHz Nortek Signature55 instrument has a vertical resolution of 20 m depth bins, and a pulsed sampling rate of six 18-second pings followed by a 4.5-minute delay. Complete datasets for Slope and Axis are averaged at a temporal resolution of 15-minutes.

To assess data quality and coverage, an initial quality check of error velocity, correlation, and backscatter intensity was performed for the raw 2-second data (not shown). For Slope, the primary analysis region is below -50 m to avoid side-lobe noise, and at Axis below -680 m to avoid instrument range limitations. The unanalysed upper depths are retained in plots, for reference.

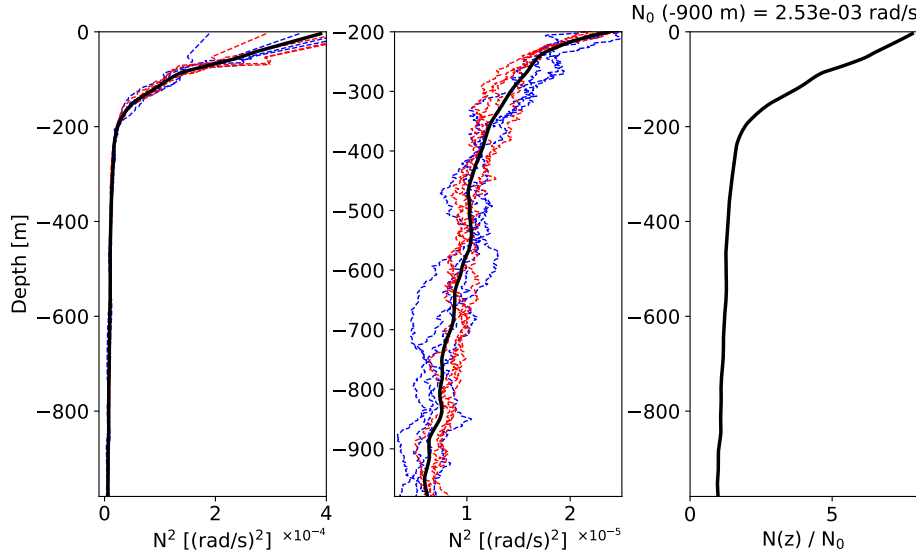


**Figure 7.**  $N^2$  parameter and WKB scaling factor. Buoyancy results were smoothed and averaged for the four analysis years at La Perouse station LB14 CTD data, and are displayed through the water column (left) and below -200 m (centre). Casts were taken in May (blue) and September (red). A WKB scaling factor (right) was determined for use in Equation 8, based on  $N_0$  averaged around -900 m.

Overlapping data coverage of good quality (e.g. minimal data gaps) is during 2013, 2014, 2017, and 2018 (Figure 5).

Additionally, there is a notable high-frequency 'hump' in the Axis power spectra. This high-frequency whitening is apparent in both the 75 and 55 kHz instruments, above about  $1.3 \times 10^{-4}$  Hz. For the Nortek 55 kHz instrument (2017 and 2018), high-frequency whitening can likely attributed to the effects of the instrument noise floor (discussed in Section 6.1.2). However, for the RDI 75 kHz instrument (2013 and 2014), the lower noise floor doesn't show noise floor effects until much further along the frequency axis, observed in spectra of the raw 2-second data. Inspection of an individual spectral window shows irregular spiking beyond about  $1.3 \times 10^{-4}$  Hz, though not consistently within the same frequency bin. Band-pass velocity data in this frequency range show irregular vertical patches a few tens of metres in scale, that appear and disappear quickly. To avoid this high-frequency noise, spectral analyses are only conducted up to  $1.2 \times 10^{-4}$  Hz. Spectral plots are shown in full, for reference.

Datasets were combined and mapped to standard depth bins. NaN values were interpolated using a linear process for gaps less than 25 hours. For large data gaps, datasets were segmented and labelled by year and section, and combined using weighted averaging when necessary. All supplemental material, includ-

ing processing code, is available in the project GitHub repository hosted at [https://www.github.com/kurtisanstey/internal\\_waves\\_barkley\\_canyon/](https://www.github.com/kurtisanstey/internal_waves_barkley_canyon/).

## 5 Methods

At Slope, horizontal velocity data were rotated using a standard rotation matrix as:

$$u_{rot} = u\cos(\theta) - v\sin(\theta) \quad (5)$$

$$v_{rot} = u\sin(\theta) + v\cos(\theta) \quad (6)$$

where  $\theta$  is the rotation angle in radians. This matches the cross-slope angle of  $\sim 30^\circ$ ;  $u$  is referred to as 'cross-slope', and  $v$  as 'along-slope' (Figure 4). At Axis, the along-canyon ( $v$ ) direction is approximately north-south, so no rotation was necessary;  $u$  at Axis is 'cross-canyon'.

To account for the effects of depth-dependent stratification, horizontal velocity data were WKB-scaled according to:

$$u_{WKB}(z) = u(z)\sqrt{\frac{N_0}{N(z)}} \quad (7)$$

and for energy density as:

$$\phi_{WKB}(z) = \phi(z)\frac{N_0}{N(z)} \quad (8)$$

with a reference buoyancy frequency of  $N_0 = 2.53 \times 10^{-3}$  rad/s averaged around -900 m (Althaus et al., 2003). Buoyancy data were determined from climatology data obtained from the nearby (21 km SE) station LB14. Data were sampled annually in May and September, during Fisheries and Oceans Canada (DFO) La Perouse cruises, casting down to -1180 m. Depth profiles were obtained for temperature, pressure, and salinity,  $S(z)$ , to find potential density,  $\rho_\theta(z)$ , following the UNESCO 1983 (EOS 80) polynomial. Depth-dependent buoyancy was then determined as in Equation 1 (Figure 7). There is little inter-annual variability in the buoyancy depth profiles.

Component-wise power spectral density (PSD) was determined from the WKB-scaled horizontal velocity data for each depth bin, using a Welch spectrogram process with a Hanning window of 256 data-points (2.7 days), 50% overlap, detrended in time to avoid a 0 Hz offset. For comparison, additional 'fine' (short window, poor frequency-resolution) and 'coarse' time-resolution (long window, greater frequency-resolution) spectra were computed with 128 (1.3

days) and 512 (5.3 days) data-points, respectively. The noise floor of each instrument was determined from the standard error of the mean relative to instrument sampling intervals and uncertainties from Nortek and RDI. 95% confidence intervals were determined using a chi<sup>2</sup> method.

For rotational dependence, rotary power spectra were determined similarly to PSD, while applying a modified spectrogram process based on the work of Gonella (1972) and Thomson and Emery (2014). To summarise, the adjustment to find the counter-clockwise (CCW) and clockwise (CW) components of a complex horizontal velocity vector,  $\mathbf{w}(t) = u(t) + iv(t)$ , is the addition or subtraction of twice its quadrature spectrum,  $Q_{uv}$ , as:

$$\text{CCW} = \frac{1}{2}[S_{uu} + S_{vv} + 2Q_{uv}] \quad (9)$$

$$\text{CW} = \frac{1}{2}[S_{uu} + S_{vv} - 2Q_{uv}] \quad (10)$$

where  $S_{uu}$  and  $S_{vv}$  are the typical complex autospectra used for PSD (Thomson & Emery, 2014). In general, a stronger CW component indicates downward propagation of energy, and vice-versa.

The open-ocean GM IW spectrum was determined following a process adapted from Callies (2016), using local parameters for  $f = 1.73 \times 10^{-5}$  Hz,  $g = 9.81(m/s)^2$ , and  $N_0$ , along with canonical values for the surface-extrapolated buoyancy frequency ( $5.24 \times 10^{-3}$  rad/s), e-folding scale of  $N(z)$  ( $1.3 \times 10^3$  m), mode scale number  $j* = 3$ , and dimensionless IW energy parameter  $E = 6.3 \times 10^{-5}$ , as in Munk and Wunsch (1981). The directional component-wise GM spectrum was adapted to rotary form through application of the rotary consistency relation, as described in Section 3 (Levine et al., 2002; Polzin & Lvov, 2011).

## 6 Results

### 6.1 Observations

#### 6.1.1 Mean currents

Regional low-frequency mean currents are inter-annually consistent, topographically guided, and seasonally site-dependent (Figure 8). To identify long-term mean currents, a 40-hour, 8th-order, digital low-pass Butterworth filter was applied to the WKB-scaled horizontal velocity data. There is little inter-annual variability in mean currents at either site. At Slope, mean currents below -40 m are as expected for this portion of the California current system (Figure 8): generally poleward along-slope (up to  $> 0.2$  m/s) through

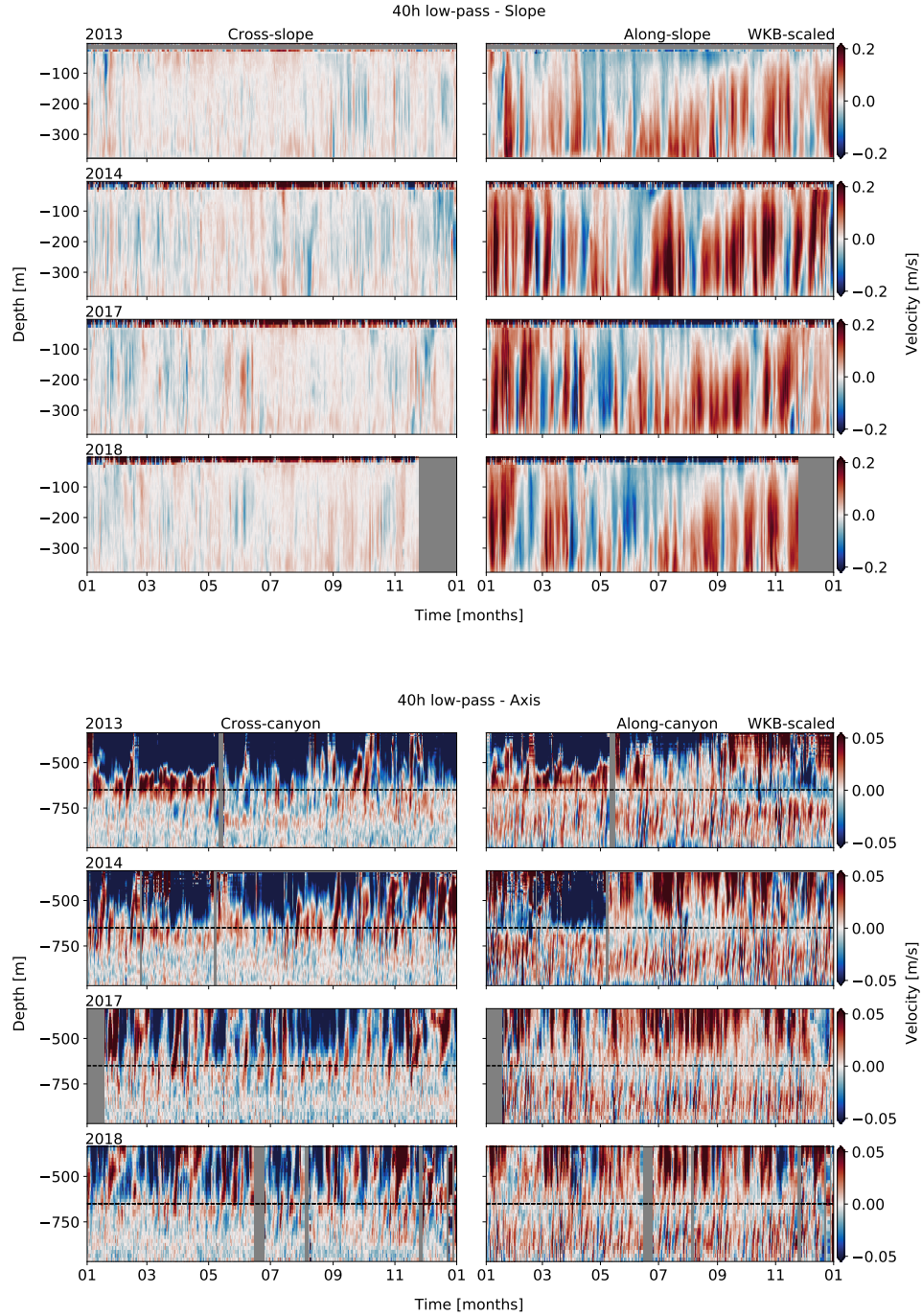


**Figure 8.** 40-hour low-pass WKB-scaled horizontal velocity data for Slope (top) and Axis (bottom). Components are separated as cross- (left) and along-slope/canyon (right). At Axis, the dashed line is the upper limit of the analysis depths (-650 m). There is a clear seasonal cycle in the along-slope component at Slope, while seasonality is less apparent in the predominantly along-canyon flow at Axis.

depth, with a quick transition to upwelling-favourable equatorward flow in the late-spring (April/May), with the deep poleward currents shoaling by fall (Thomson et al., 2015). In the canyon, mean currents within analysis depths (below -680 m) are seasonally consistent up-canyon (up to  $> 0.05$  m/s), with down-canyon flow  $< 50$  m AB (Figure 23). A two-week rolling depth-average (between about -700 and -900 m) gives inter-annually consistent positive (up-canyon) velocities up to 0.02 m/s, with annual means ranging between 0.007 - 0.010 m/s. A two-layer flow system was noted in biological studies at Barkley Canyon (Cabrera et. al, 2018; Chauvet et al., 2018), and in Monterey Canyon (Xu and Noble, 2009), and attributed to canyon circulation cells due to along-canyon pressure gradients caused by long-term large-scale along-shelf regional currents. Near-bottom ( $< 60$  m) down-canyon flow has been linked to turbidity currents and river-flood-induced underflows, that occur as shelf sediment descends through canyons to the ocean interior (Xu and Noble, 2009; Chauvet et al., 2018). Tidal rectification, where an up-slope pressure gradient is driven by tidal forcing (Garrett, 2005), could also force a mean up-canyon flow cycle.

### 6.1.2 High-pass currents

High-frequency (40-hour high-pass) velocity data show variability in constituent IW and IT. Subtracting the low-pass currents from the total yields residual 'high-pass' currents - flows with periodicity less than 40-hours (Figure 9). A two-week snapshot of the higher-frequency velocities during the annually recurring spring mean-current transition reveals the presence of IW and IT of various frequencies and non-uniform vertical structure, suggesting some baroclinic forcing. There is some variability both inter-annually and seasonally, though it is difficult to distinguish. At the Slope site, high-pass currents reach over 0.1 m/s in both cross- and along-slope directions, suggesting less topographic (along-slope) guidance than for mean-currents, and there is notable non-uniform vertical structure above -250 m depth (about 150 m AB). At Axis, high-pass currents are strongest below -750 m (about 250 m AB), up to about 0.2 m/s and mostly along-canyon, with increased non-uniformity in the vertical structure above.

Annual mid-depth (-195 m and -800 m) power spectra at each site are characteristically red, and show strong tidal and NI influence (Figure 10). Inter-annual variability is minimal, with annual spectra overlapping within the 95% confidence interval. Primary tidal constituents are of the diurnal ( $1.16 \times 10^{-5}$  Hz) and semidiurnal ( $2.24 \times 10^{-5}$  Hz) frequencies, bordering the NI peak ( $1.73 \times 10^{-5}$  Hz). Closely associated constituents (such as  $S_2$  and  $M_2$ ) are not resolved due to spectral averaging, so the tidal peaks are referred to generally (e.g. diurnal). The low-frequency 'sub-diurnal' broadband ranges below

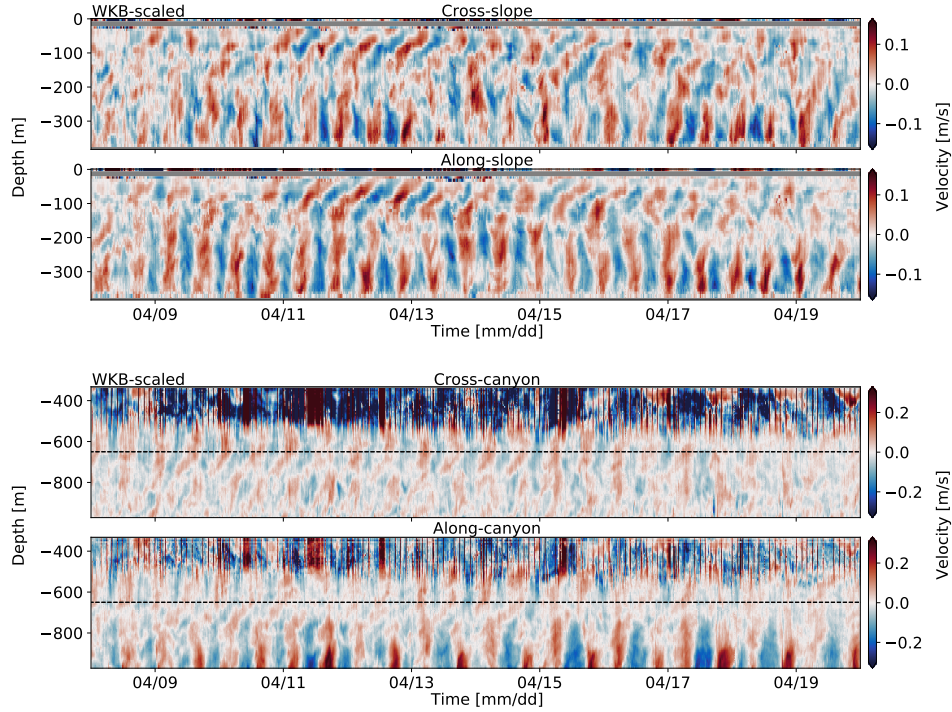


**Figure 9.** 40-hour high-pass WKB-scaled horizontal velocity data for Slope (top) and Axis (bottom), in April 2013. Components are separated as cross- (left) and along-slope/canyon (right). There are IW and IT of varied frequency, non-uniform vertical structure, and depth-dependence.

about  $1 \times 10^{-5}$  Hz. The high-frequency IW 'continuum' band (between  $7 \times 10^{-5}$  and  $1.2 \times 10^{-4}$  Hz) ranges between the  $M_6$  spectral sum peak and the noise floor affected portion of the Axis 55 kHz spectra.

At Slope, the mid-depth power spectra are similar to previous observations on the VICS (Thomson et al., 1990; Allen et al., 2001). Tidally, the semidiurnal peak is the strongest along-slope constituent (about  $2 \times 10^2$  (m/s) $^2$ /Hz), while the diurnal peak is stronger cross-slope (about  $1.5 \times 10^2$  (m/s) $^2$ /Hz). The NI peak is of similar strength in both directions (about  $1.5 \times 10^2$  (m/s) $^2$ /Hz). The sub-diurnal broadband is strongest along-slope, with strength increasing inversely to frequency. Above the minor sum-frequency peaks ( $fM_2$ ,  $M_4$ , etc.), the continuum trails off slightly whiter than the expected open-ocean GM slope of -2, mostly cross-slope, with effects from the noise floor becoming apparent near  $N$  (apparent in high frequency-resolution spectra, not shown). All frequency bands are strongest in the CW rotary component, particularly the NI constituent, as expected for the northern hemisphere.

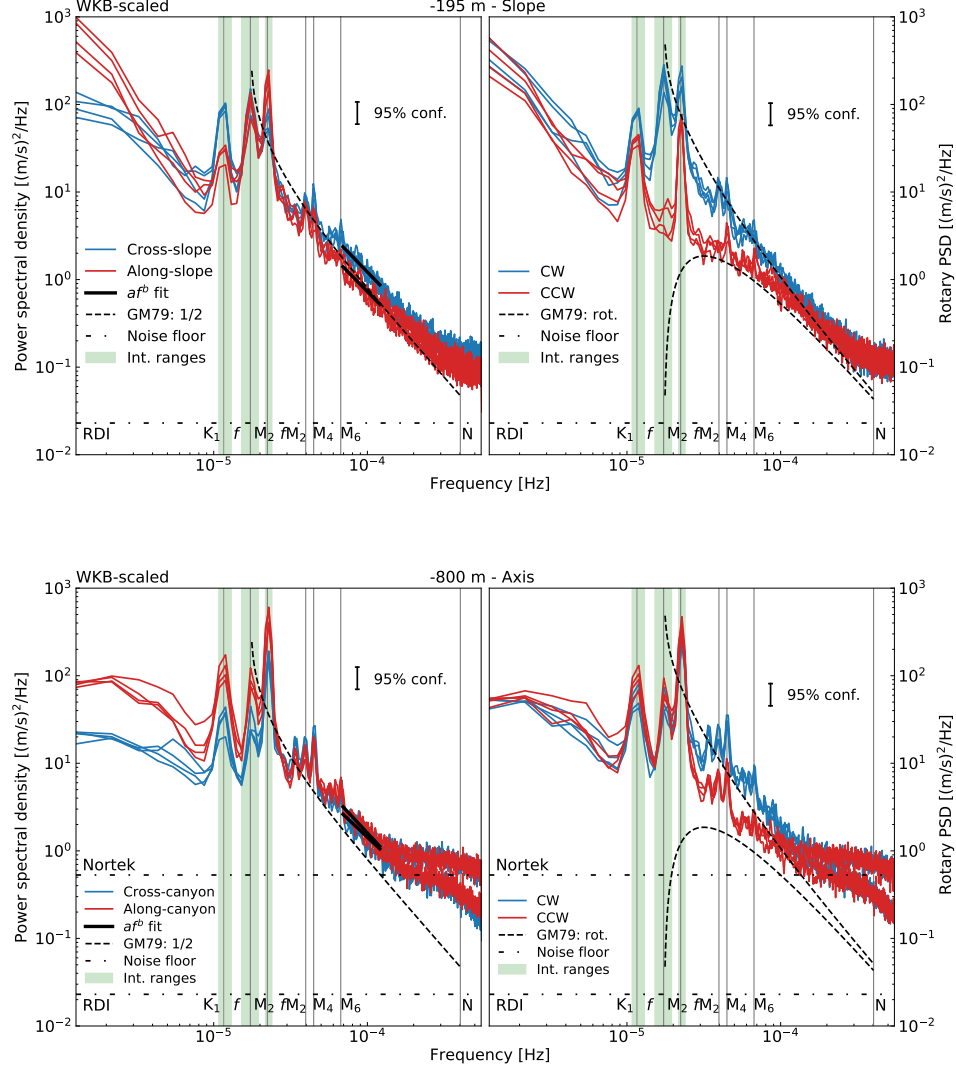


**Figure 10.** Mid-depth annual PSD (left) and rotary (right) spectra of WKB-scaled horizontal velocity data, for Slope (top) and Axis (bottom). For PSD, cross- (blue) and along-slope/canyon (red) components are shown; for rotary, CW (blue) and CCW (red) components are shown. 95% confidence intervals are indicated by the black bar. Instrument noise floors (dotted line) and primary frequency constituents with integration range (vertical lines and green shading) are shown. For PSD, black lines indicate continuum power-law fIT, and the dashed line is the GM79 spectrum (1/2 amplitude). For rotary, the GM79 spectrum is in rotary components (CW upper). Spectra at both sites are characteristically red, with prominent tidal and NI peaks.

At Axis, the sub-diurnal, tidal, and NI power trends toward along-canyon, rectilinear components, suggesting topographic guiding of flow. Compared to

Slope, the Axis sub-diurnal range is somewhat weaker at IT low end, while the rest of the spectrum appears slightly more energetic than on the slope, with a whiter continuum and a notable high-frequency 'hump' approaching  $N$  that is likely instrument noise (as discussed in Section 4).

## 6.2 Depth dependence

At each site, there is adjustment of spectral power near-topography that is frequency-dependent. The WKB-scaled PSD and rotary spectra were time-averaged in an annual 2D depth-frequency analysis (Figures 11 and 12), and results show a general increase (or decrease for NI at Slope) in spectral power (over an order of magnitude) in a concentrated layer (< a few hundred metres) above the bottom. Intensified near-slope layers are not uncommon, and are usually driven by focused incident IW energy that enhances up-slope flow (Polzin et al., 1997; Nash et al., 2004; Kunze et al., 2012). Hotchkiss and Wunsch (1982) found a  $\sim 10\times$  increase in near-slope IW energy near Hudson Canyon, with a depth-dependent vertical scale of about 150 m AB at -400 m depth.

At Slope (Figure 11), the sub-diurnal, tidal, and continuum bands show near-slope intensification, while the NI band is attenuated near the slope, generally below -200 m depth (about 150 m AB). The sub-diurnal band shows intensification in mostly the along-slope and rectilinear rotary components. The diurnal band shows intensification in mostly the along-slope and CCW components, while the semidiurnal and continuum bands show intensification that is fairly equally distributed directionally and mostly CW. There is near-slope attenuation in the NI band that is most evident in the CW component. The enhancement in the continuum band is also stronger CW.

At Axis (Figure 12), most frequencies constituents display rectilinear, along-canyon near-bottom enhancement, generally below -700 m depth (about 250 m AB). The sub-diurnal, diurnal, and NI intensification is entirely along-canyon, with little to no power in the cross-canyon direction. The NI band, in contrast to Slope, has bottom-intensified flow that is almost entirely along-canyon. The semidiurnal intensification is strongly along-canyon, but with a medium-strength cross-canyon signal that is sharply attenuated below about 100 m AB. Continuum enhancement is mostly along-canyon.

Qualitatively, at Slope the near-bottom enhanced layer is most prominent up to about 150 m AB, and at Axis up to about 250 m AB. However, the sub-diurnal band shows enhancement of up to an additional 50 m vertical. A vertical scale analysis of the topography-enhanced bottom layer was performed for each site, and results generally agree with the qualitative observations. Gemmrich

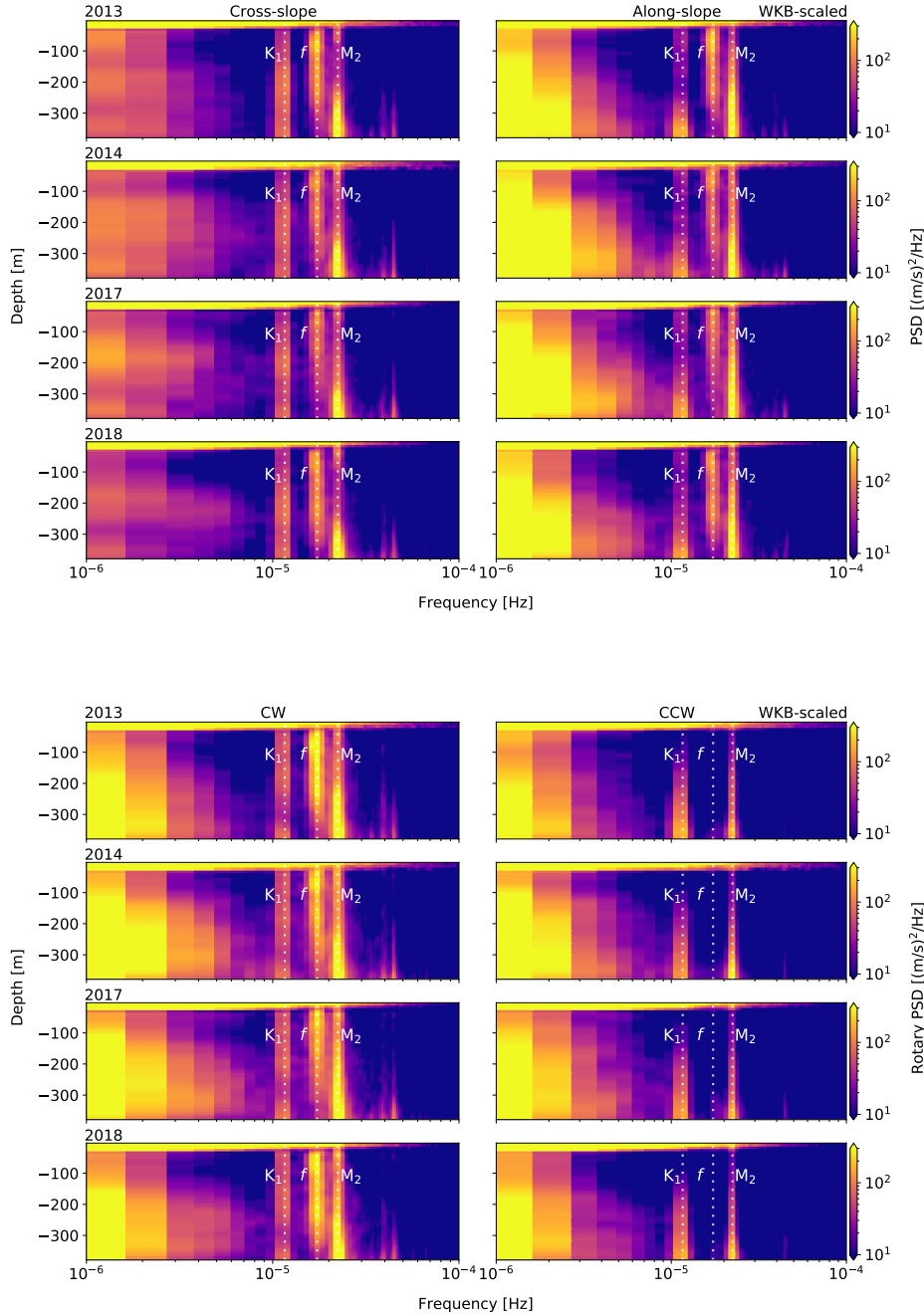


**Figure 11.** Depth-frequency PSD (top) and rotary spectra (bottom) for Slope. Components are separated as cross-/CW (left) and along-slope/CCW (right). Determined from WKB-scaled horizontal velocity data. There is near-bottom intensification of individual frequency constituents (and near-bottom attenuation of the NI band).

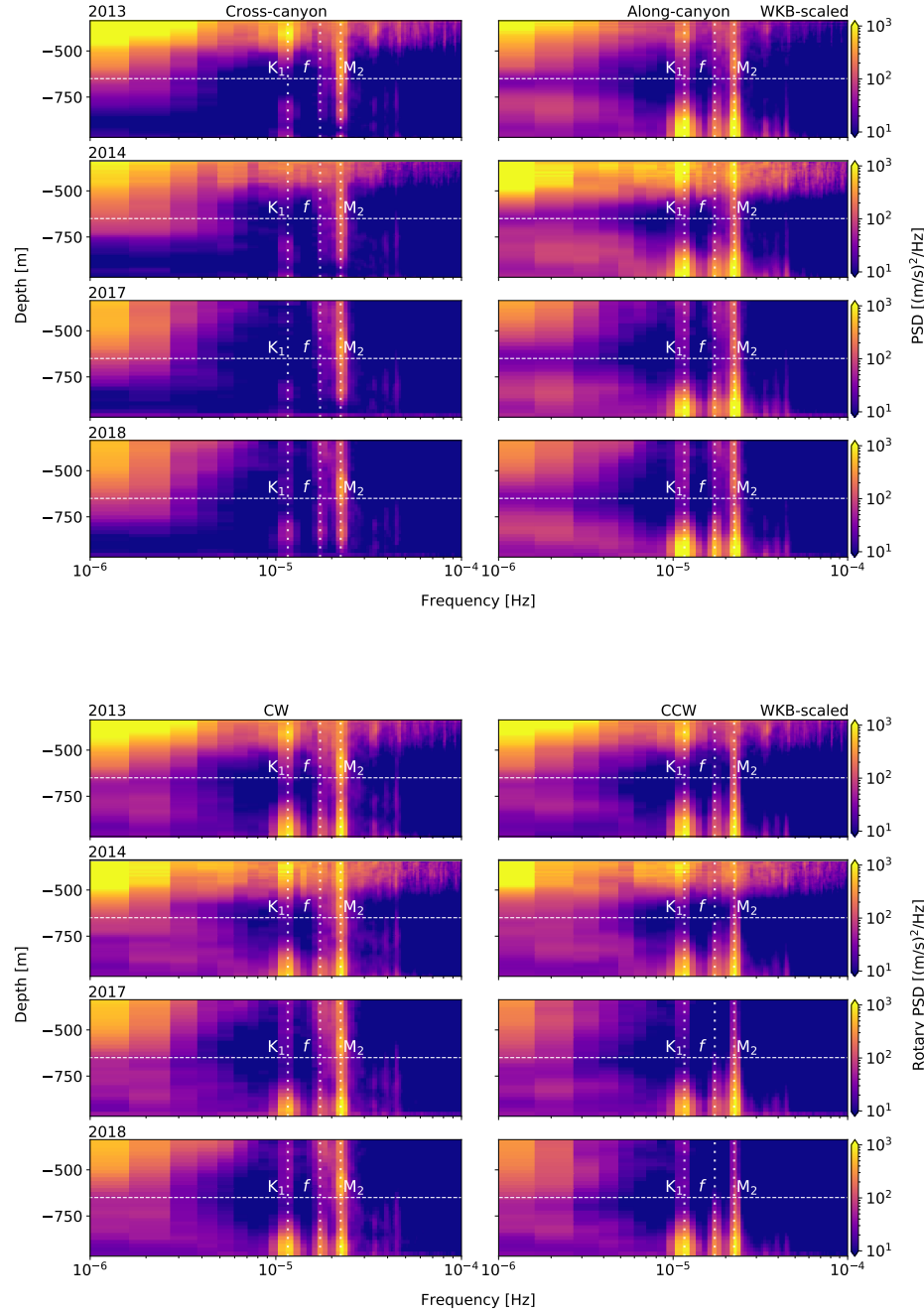


**Figure 12.** Depth-frequency PSD (top) and rotary spectra (bottom) for Axis. Components are separated as cross-/CW (left) and along-canyon/CCW (right). Determined from WKB-scaled horizontal velocity data. Dashed line indicates upper depth limit for analysis. There is near-bottom intensification of individual frequency constituents.

and Klymak (2015) found that mode-1 IW incident on sloped topography can induce a near-bottom turbulent flow layer, and that the vertical scale of the effect can be approximated as:

$$H \approx \frac{\pi U}{N} \quad (11)$$

where  $U$  is the forcing by cross-slope velocity. For strong velocity forcing within 100 m AB (from high-pass observations) and approximate buoyancy values for near-topography depths at Slope ( $U \approx 0.15$  m/s;  $N \approx 3.5 \times 10^{-3}$  rad/s at -350 m) and Axis ( $U \approx 0.25$  m/s;  $N \approx 2.5 \times 10^{-3}$  rad/s at -900 m), estimates result in vertical scales of about 135 m and 314 m, respectively. These estimates are similar to the qualitative observations at Slope, and somewhat greater at Axis, and agree with the results of Gemmrich and Klymak (2015) for enhanced bottom-layer flow with similar forcing and stratification; however, they do not account for adjusted stratification near topography (due to the CTD climatology data being from a nearby open-ocean site). *Expand on near-bottom intensification.*

### 6.3 Frequency dependence and seasonality

There is frequency-dependent variability in the intensity and seasonality of the observed enhancement layer (and attenuation for NI at Slope). Little inter-annual variability is observed, notable only in the intermittent sub-diurnal and NI seasonality. WKB-scaled PSD and rotary spectra were integrated over bandwidths covering each constituent peak or broadband (shown as shaded regions in Figure 10), at each depth bin, resulting in depth-band power plots. Constituent frequency ranges are sub-diurnal ( $\leq 1.08 \times 10^{-5}$  Hz), diurnal ( $1.08\text{--}1.30 \times 10^{-5}$  Hz), NI ( $1.52\text{--}1.95 \times 10^{-5}$  Hz), semidiurnal ( $2.17\text{--}2.39 \times 10^{-5}$  Hz), and the continuum ( $7.00 \times 10^{-5} \text{--} 1.20 \times 10^{-4}$  Hz).

#### 6.3.1 Sub-diurnal and diurnal

For the broadband sub-diurnal range, near-topography enhancement is approximately  $1.5\times$  orders of magnitude at Slope, and  $2\times$  orders of magnitude at Axis (Figures 13 and 14). At Slope, the enhancement layer is most prominent in the along-slope and CW components, while at Axis the enhancement is mostly along-canyon and rectilinear. Theory dictates that propagation of sub-inertial sub-diurnal IW should be restricted to along-topography flow at this latitude (Flather, 1988), as observed.

Sub-diurnal enhancement layer seasonality at Slope consists of intermittent pulses in both the fall and winter, and is one of few observations that is not inter-annually consistent. At Axis, seasonality is weak, showing only an

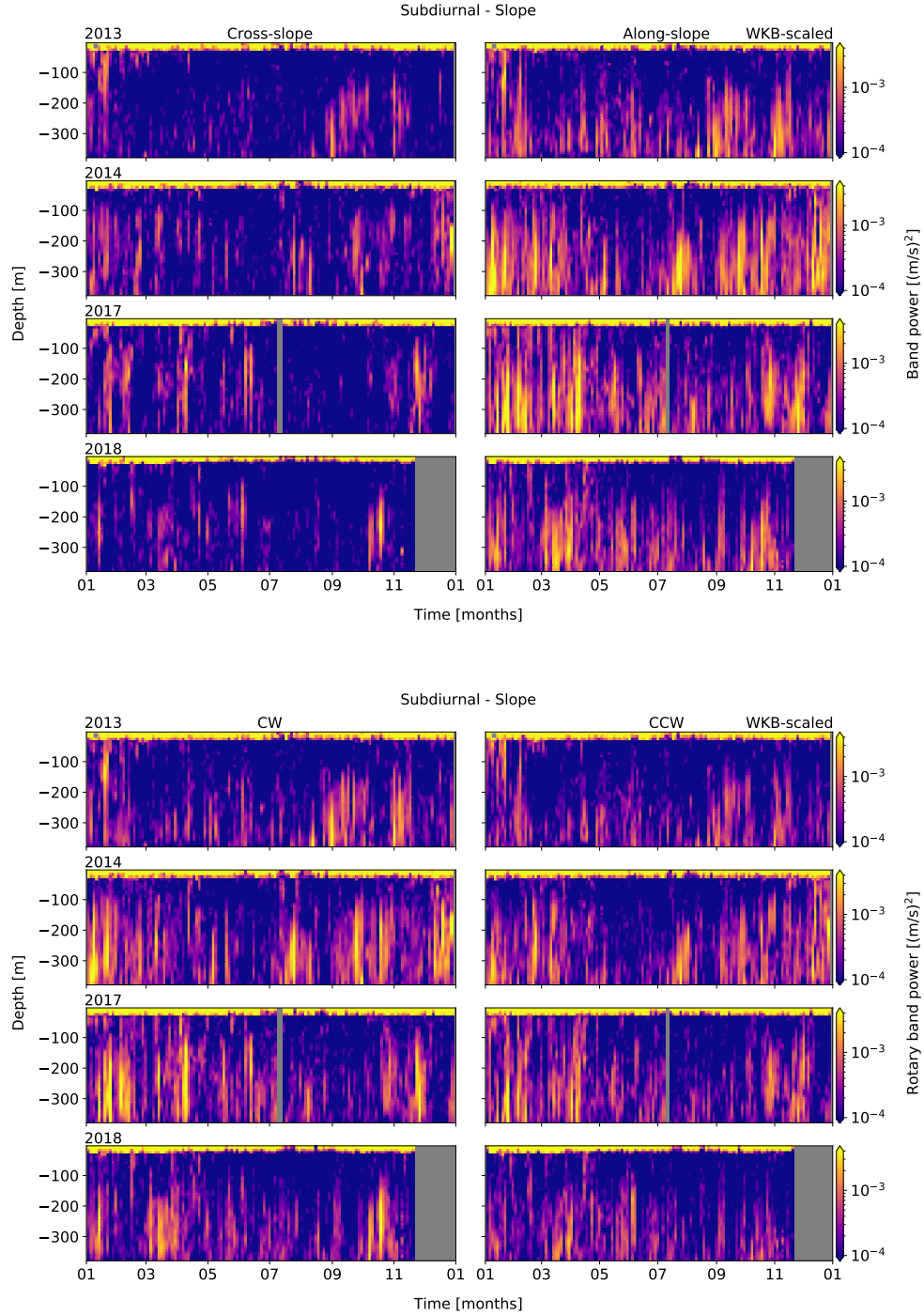


**Figure 13.** Band-integrated sub-diurnal PSD (upper) and rotary (lower) spectra for Slope, from WKB-scaled horizontal velocity data. Cross- (left) and along-slope (right) components are shown. Each row represents an analysis year, labelled at upper-left.

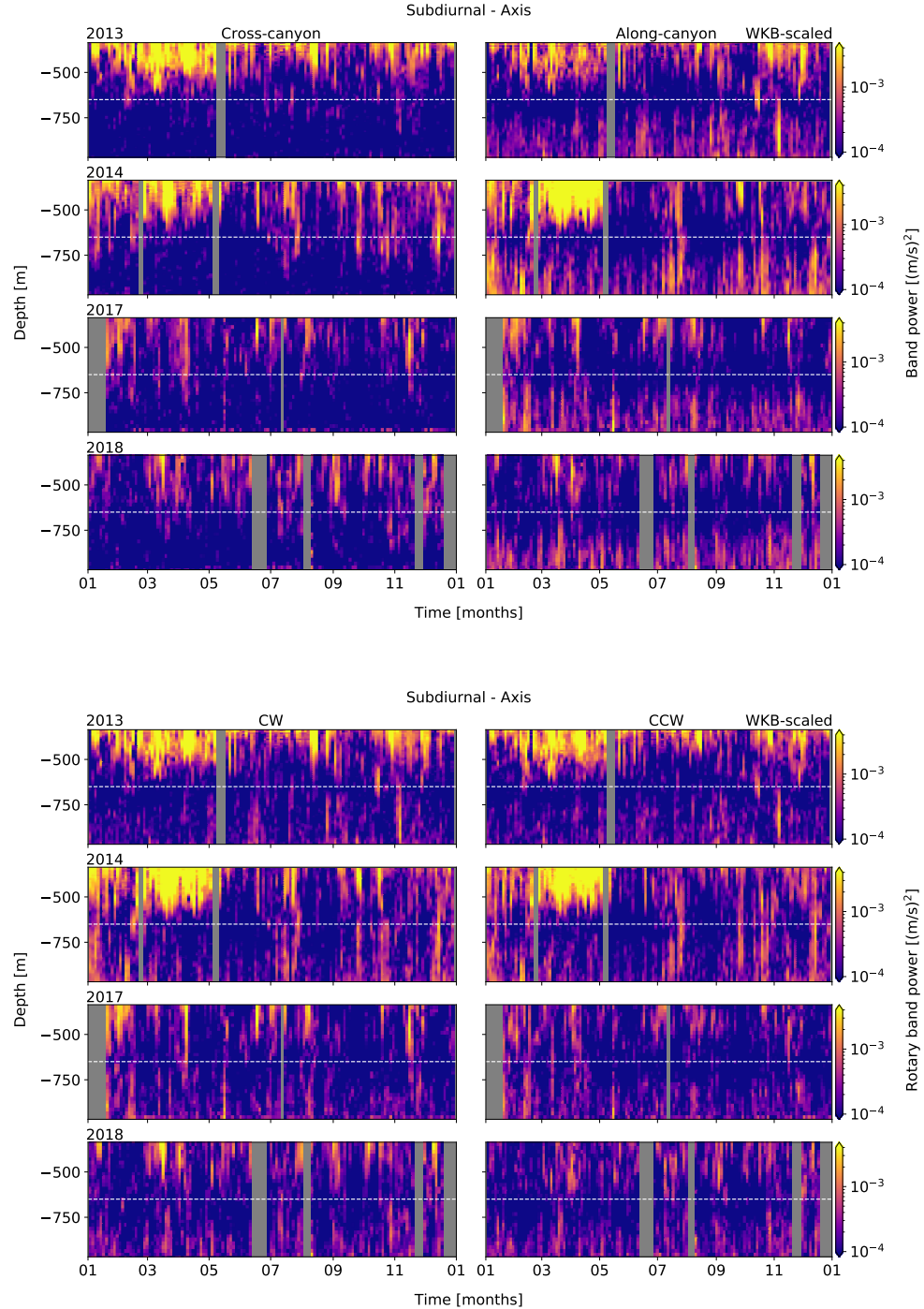


**Figure 14.** Band-integrated sub-diurnal PSD (upper) and rotary (lower) spectra for Axis, from WKB-scaled horizontal velocity data. Cross- (left) and along-slope (right) components are shown. Each row represents an analysis year, labelled at upper-left.

occasional fall pulse. Though sub-diurnal motions are often linked to mean-currents (Cummins et al., 2000), few seasonal features are common to both. Comparisons with other frequency bands show a similar lack of common features, at both sites. Low-frequency motions can be affected by a variety of sub-tidal physical processes near slope, shelf, and canyon topography, and a forcing analysis for the sub-diurnal range is beyond the scope of this paper. However, the presence of seasonal sub-diurnal energy will be considered when evaluating forcing of other frequency constituents. *Expand this!*

For the diurnal constituent, the near-topography enhancement is approximately  $1.5\times$  orders of magnitude at Slope, and  $2\times$  orders of magnitude at Axis (Figures 15 and 16). There is vertically linear uniformity that is indicative of primarily local barotropic forcing, at both sites. At Slope, the enhancement layer is most prominent in the along-slope and CCW components, while at Axis the enhancement is mostly along-canyon and rectilinear. As the diurnal (and sub-diurnal) frequency is sub-inertial, it is unlikely for there to be incident baroclinic diurnal IW unless they propagate along the shelf. The diurnal constituent is sub-inertial at this latitude (as is the sub-diurnal range), and the mostly along-topography result is similar to other Pacific slopes (Rudnick, 2015) and seamounts (Robertson et al., 2017). Cummins and Oey (1997) found that sub-inertial diurnal IT generation was prevalent on the VICS adjacent continental slope, but that motions were evanescent (trapped) along-slope, unable to radiate offshore as they are restricted north of their turning latitude ( $\sim 30^{\circ}\text{N}$ ).

Diurnal enhancement seasonality at Slope is consistent inter-annually, showing a regular pulse beginning late-spring through summer (( $\sim$ May - August) and a weaker pulse in the fall/early-winter ( $\sim$ November - January), while seasonality at Axis is not readily apparent. Drakopolous and Marsden (1993) associated strengthened diurnal tidal flow over the VICS with increased stratification in summer, while Cummins et al. (2000) suggest that diurnal tidal currents over the VICS are seasonally responsive to the large-scale spring shift to equatorward upwelling-favourable mean currents, a consistent inter-annual process in the region. Similar results were noted by Xu and Noble (2009), who found inter-annually consistent  $K_1$  currents in Monterey Canyon, that peaked relative to the annual cycle of spring/neap-tide forcing.

### 6.3.2 Near-inertial

For NI, the near-bottom attenuation at Slope is approximately  $1.5\times$  orders of magnitude, compared to upper-depth amplitudes (Figure 17). The near-bottom enhancement layer at Axis is about  $2\times$  orders of magnitude (Figure 18). At Slope, NI power is greatest near the surface, evenly distributed di-

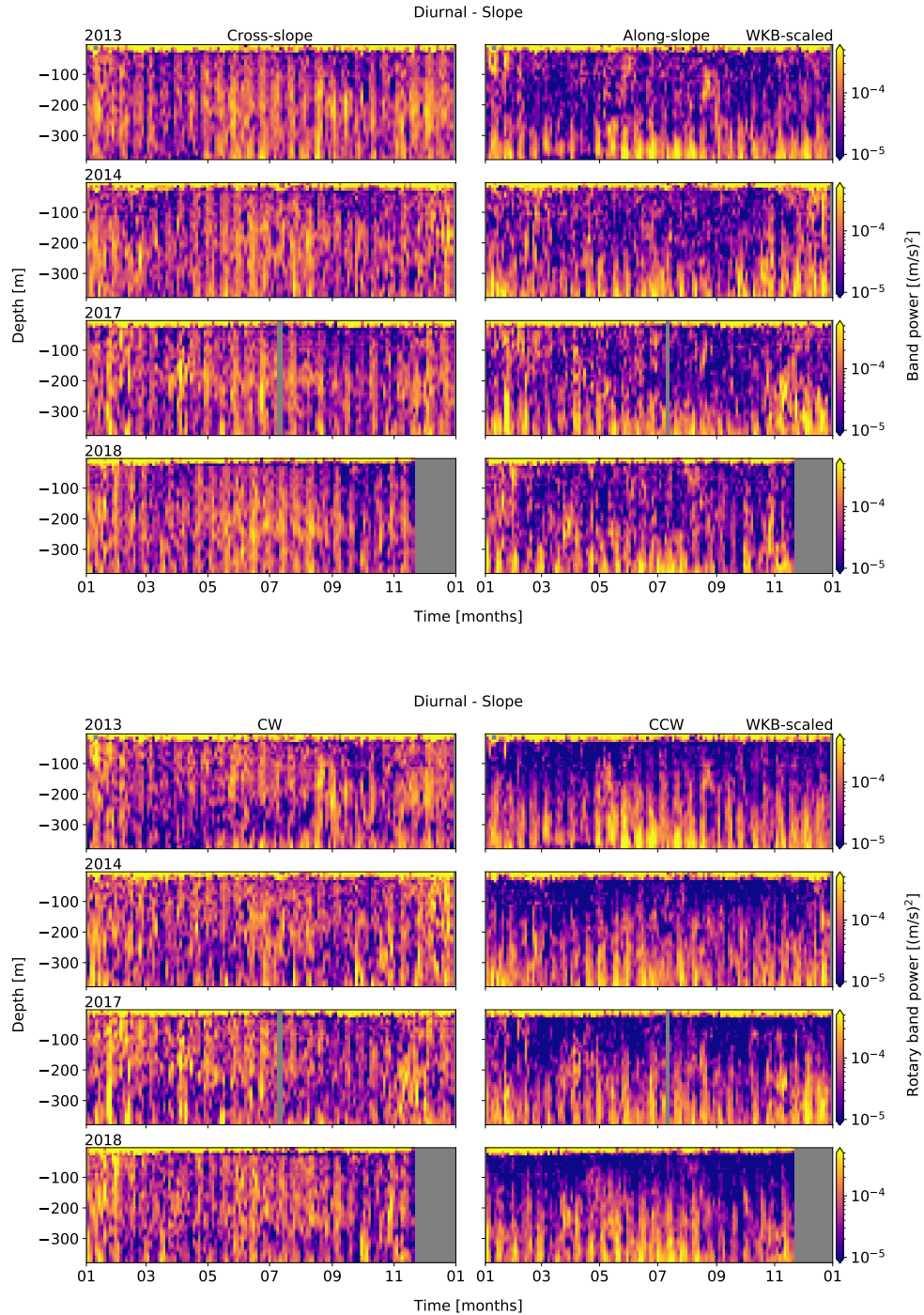


**Figure 15.** Band-integrated diurnal PSD (upper) and rotary (lower) spectra for Slope, from WKB-scaled horizontal velocity data. Cross- (left) and along-slope (right) components are shown. Each row represents an analysis year, labelled at upper-left.

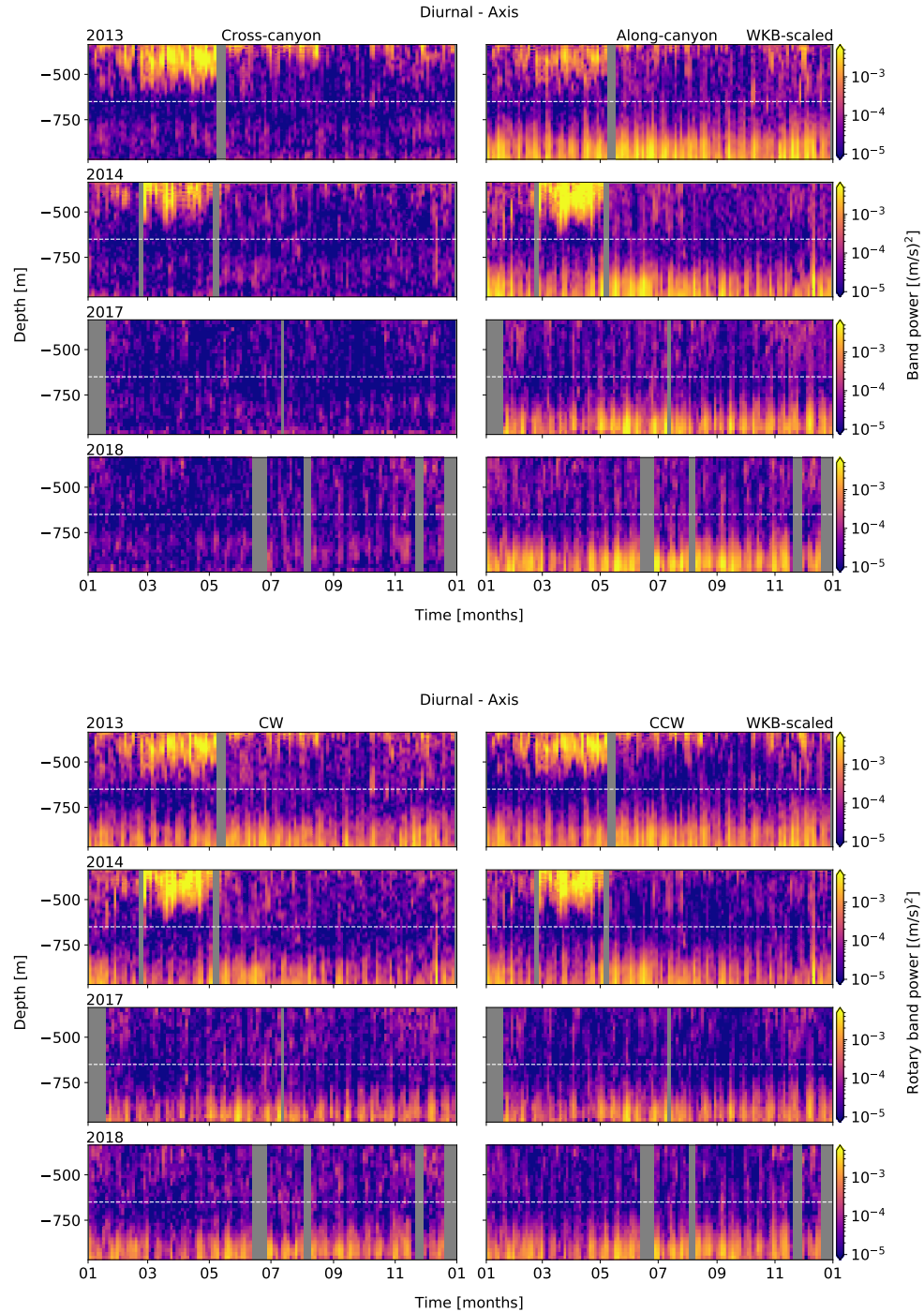


**Figure 16.** Band-integrated diurnal PSD (upper) and rotary (lower) spectra for Axis, from WKB-scaled horizontal velocity data. Cross- (left) and along-slope (right) components are shown. Each row represents an analysis year, labelled at upper-left.

rectionally and entirely CW (downward propagation is expected for NI IW generated at the surface), down to about 150 m AB where attenuated begins. At Axis, the near-bottom enhancement layer is mostly along-canyon and rectilinear up to about 250 m AB. Thomson et al. (1990) found that NI IW become increasingly attenuated as they approach slopes, absorbed by strong vertical shear in the background flow associated with topographically trapped oscillations.

At Slope, NI seasonality above the attenuation region is highly intermittent, with pulses most likely in the fall and early-winter, though they may occur year-round. At Axis, generally only the significant fall and early-winter events from Slope are evident. General seasonality is inter-annually consistent, while specific events are not. Intermittent forcing of NI IW is common; small ( $\sim$  100 km) southward cold fronts and lows with considerable CW NI rotation are the most significant sources of NI flux, more-so than even synoptic scale systems, and occur most often in fall and early-winter (D'Asaro, 1985; Alford, 2001; Voelker, 2020). Additionally, seasonal pycnocline and mixed-layer (ML) depths have been observed to modulate NI energy by up  $12\times$  when thin, by affecting stratification-dependent modes 'strummed' by ML NI currents which generate NI IW through divergent 'pumping' at the ML base (Jarosz et al., 2007).

For prominent seasonal pulses at Slope, there are periods of downward propagation of NI energy from the ML (above -40 m) to about -100 m, lasting up to about two weeks, after which the deep response appears to quickly increase. At Axis, the timing of pulses appears to correspond to that of the deep response observed at Slope. This initial propagation period has been associated with the separation of the first few modes (Gill, 1984; D'Asaro, 1995), described as 'inertial beating', where the horizontal departure of each mode leads increases vertical propagation of NI energy (Zervakis and Levine, 1995). Time-scales for the departure of mode-1 and mode-2 are associated with a transfer of NI energy from the ML to the upper-pycnocline, up to 10-20 days, after which the deep response increases and NI energy is evenly distributed in the pycnocline and lower depths (Zervakis and Levine, 1995). This quick radiation to deep water is associated with 'inertial jets' of CW relative vorticity originating near the upper pycnocline, possibly induced by mesoscale fronts (Kunze, 1985; D'Asaro, 1995; Zhai et al., 2005; Alford et al., 2016).

### 6.3.3 Semidiurnal

For the semidiurnal constituent, the near-topography enhancement is approximately  $2\times$  orders of magnitude at Slope, and  $3\times$  orders of magnitude at Axis (Figures 19 and 20). At Slope, the enhancement layer is evenly distributed

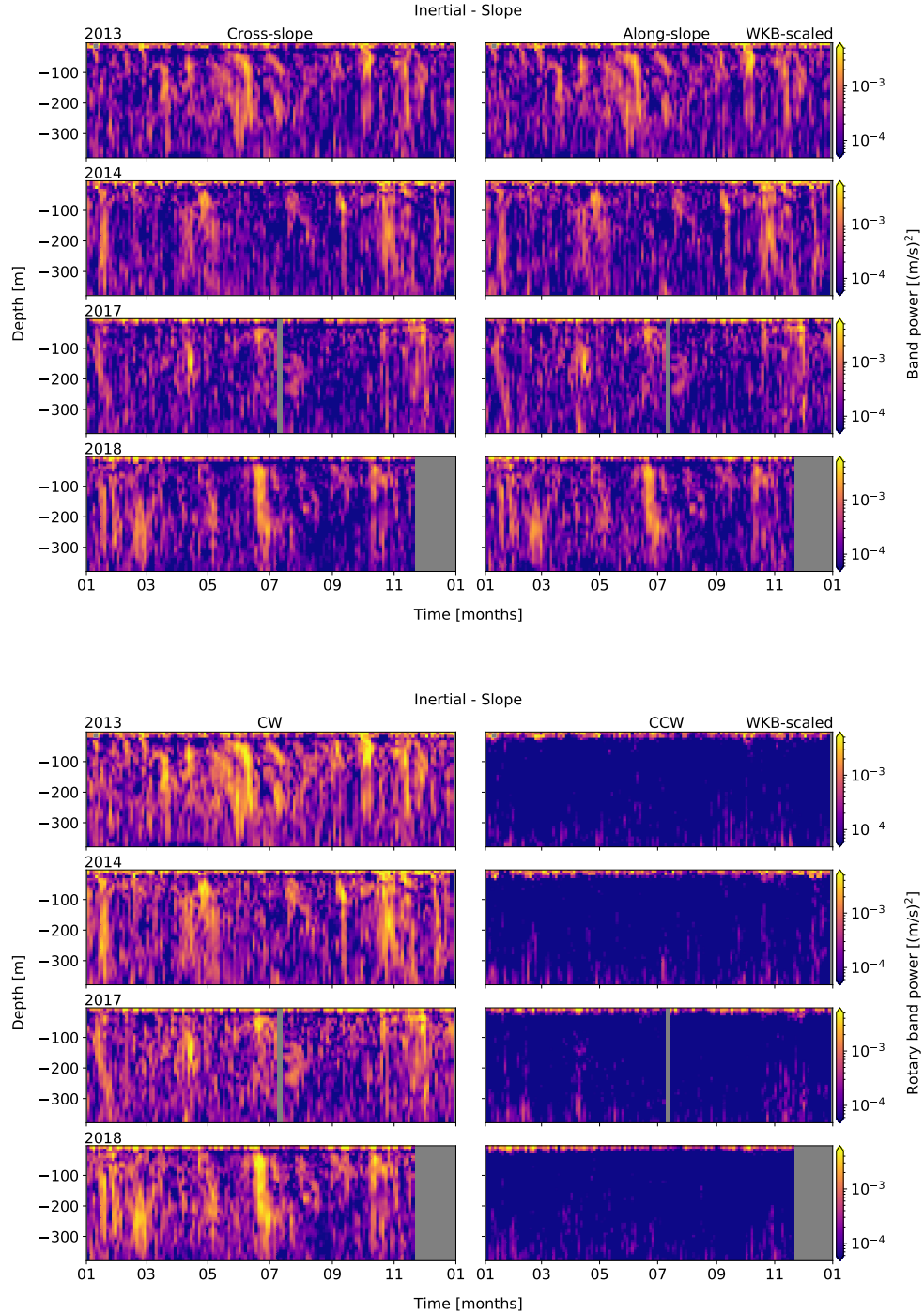


**Figure 17.** Band-integrated NI PSD (upper) and rotary (lower) spectra for Slope, from WKB-scaled horizontal velocity data. Cross- (left) and along-slope (right) components are shown. Each row represents an analysis year, labelled at upper-left.

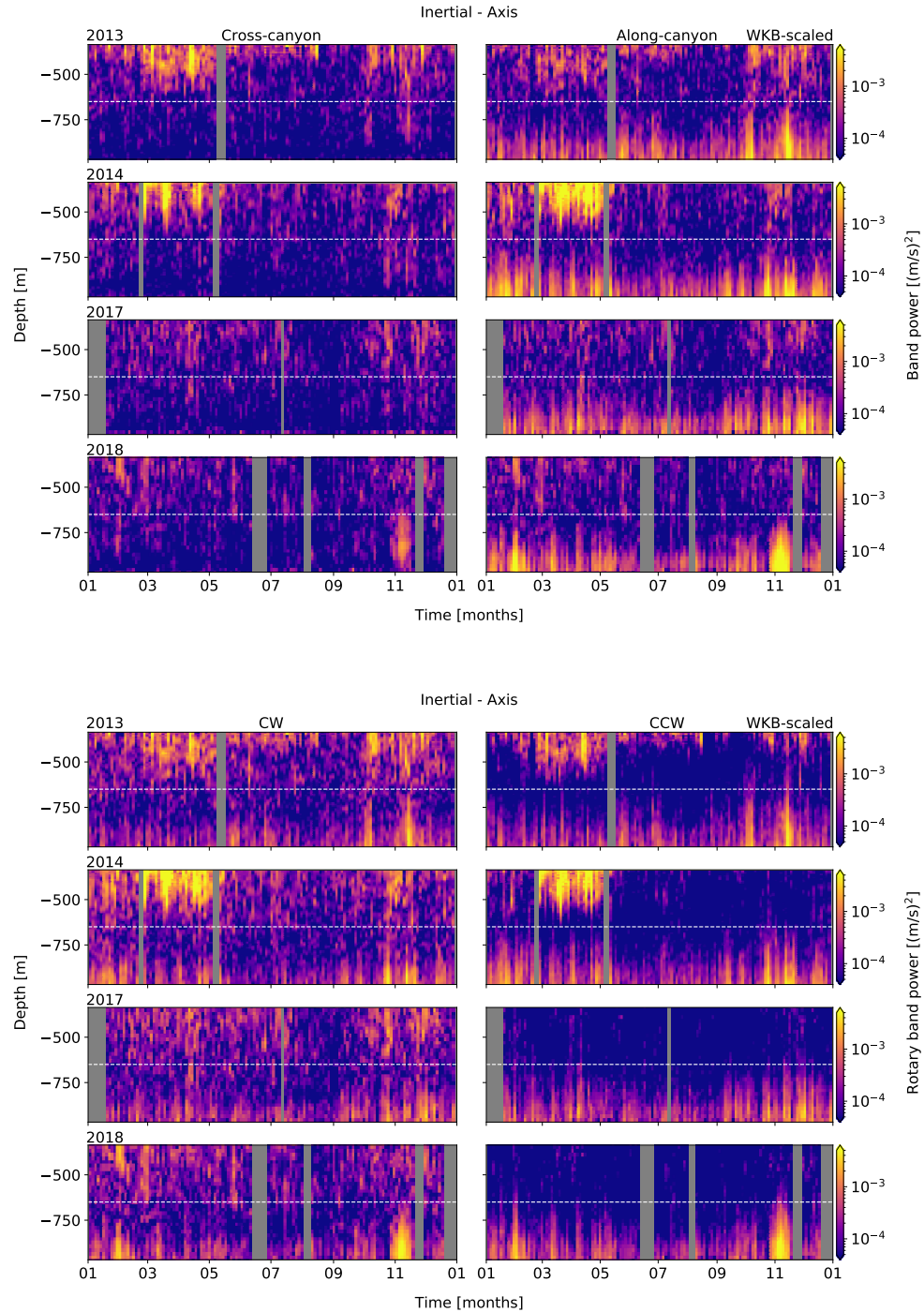


**Figure 18.** Band-integrated NI PSD (upper) and rotary (lower) spectra for Axis, from WKB-scaled horizontal velocity data. Cross- (left) and along-slope (right) components are shown. Each row represents an analysis year, labelled at upper-left.

directionally and entirely CW up to about 150 m AB, while at Axis the enhancement is mostly along-canyon and rectilinear up to about 200 m AB. This is not surprising, as it has been shown that where criticality ( $\beta/\alpha$ , as detailed in section 3) is near to 1, typically below the shelf-break, incident semidiurnal IT are most strongly subject to near-slope focusing and reflection (Robertson et al., 2017). At other slope sites, there is evidence of elevated near-bottom energy-flux associated with both semidiurnal IT generation and incident reflection, with topographically dependent vertical scales within a few hundred metres AB (Terker et al., 2014; Xie and Chen, 2021). Locally, Drakopoulos and Marsden (1993) found that seaward of the VICS shelf break that semidiurnal IT propagation was strongly CW downward - noted at other slope sites (Subeesh et al., 2021) - and attributed to incident IT downward reflection and seaward generation from the shelf and near-critical shelf-break.

Semidiurnal enhancement layer seasonality at Slope is inter-annually consistent and subtle, showing a slight pulse that begins in the late-spring/early-summer (months 4/5) and an even weaker pulse in the fall/early-winter. Seasonality at Axis is not readily apparent. Drakopoulos and Marsden (1993) found that the semidiurnal IT on the VICS continental margin gained strength in the late-spring through summer, attenuating by September, associated with seasonal changes in stratification.

#### 6.3.4 Continuum

For the high-frequency IW continuum, near-topography enhancement is approximately 1× orders of magnitude at Slope, and 1.5× orders of magnitude at Axis (Figures 21 and 22). At Slope, the enhancement layer is mostly cross-slope and CW, up to about 150 m AB, while at Axis the enhancement is evenly distributed directionally and mostly CW, up to about 200 m AB.

Continuum enhancement layer seasonality at Slope is inter-annually consistent, showing a pulse in the spring that lasts through early-summer, and another through the fall. At Axis, seasonality is less apparent, with only a few fall pulses from Slope showing up in the canyon. IW energy is known to cascade from low- (tidal and sub-tidal) to high-frequency (continuum) processes, with continuum seasonality reflecting such a transfer of energy (Polzin, 2004).

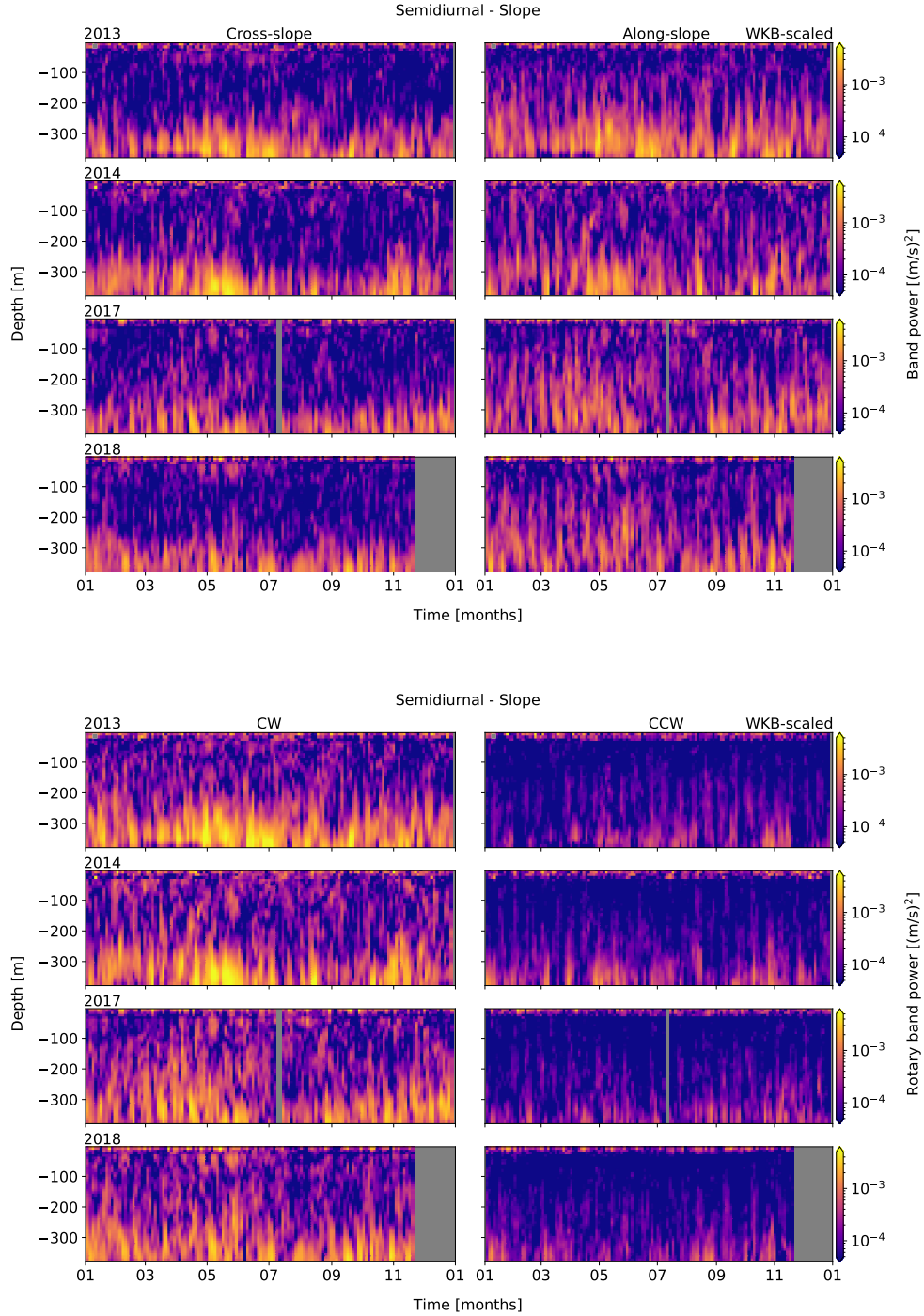


**Figure 19.** Band-integrated semidiurnal PSD (upper) and rotary (lower) spectra for Slope, from WKB-scaled horizontal velocity data. Cross- (left) and along-slope (right) components are shown. Each row represents an analysis year, labelled at upper-left.

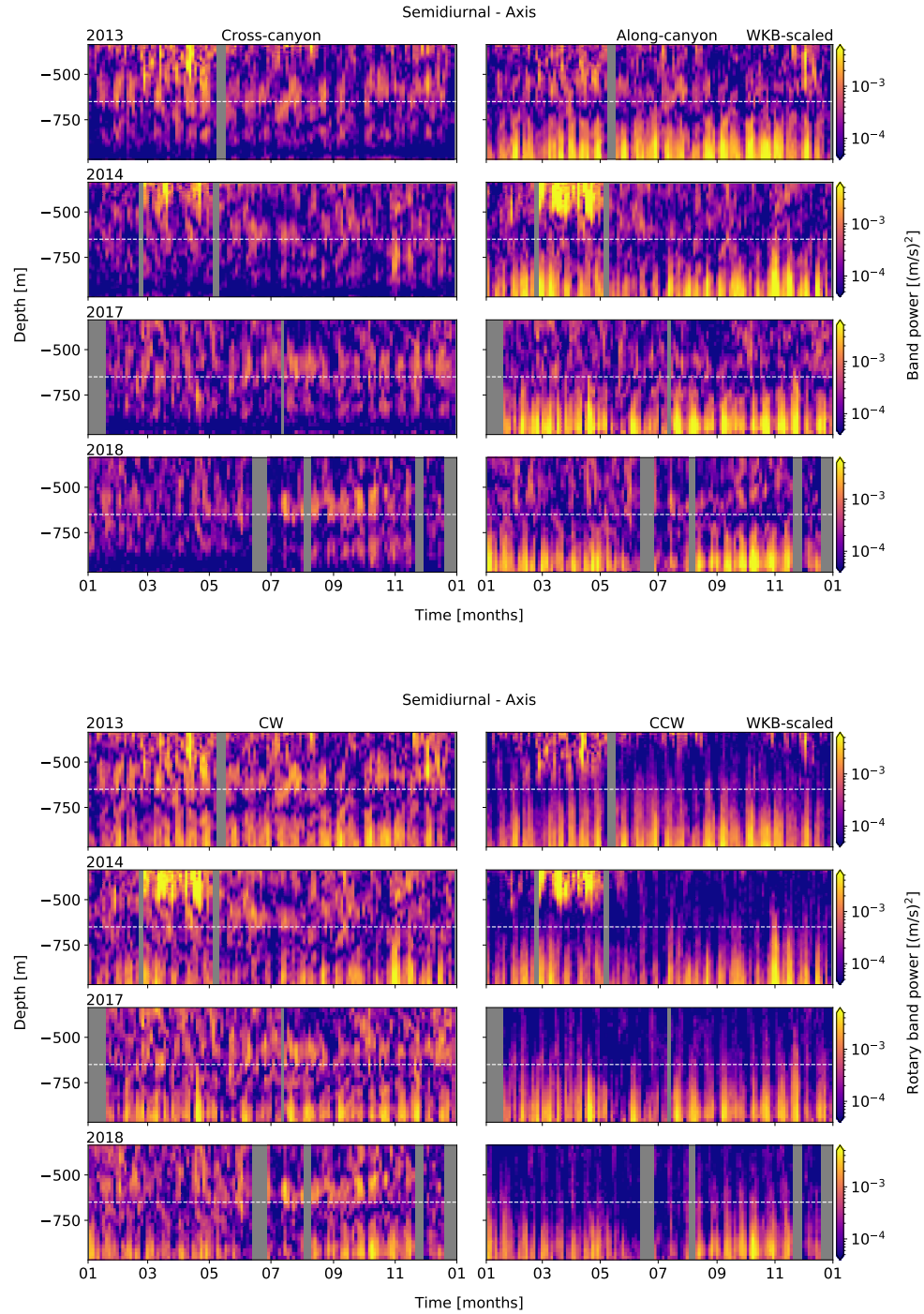


**Figure 20.** Band-integrated semidiurnal PSD (upper) and rotary (lower) spectra for Axis, from WKB-scaled horizontal velocity data. Cross- (left) and along-slope (right) components are shown. Each row represents an analysis year, labelled at upper-left.

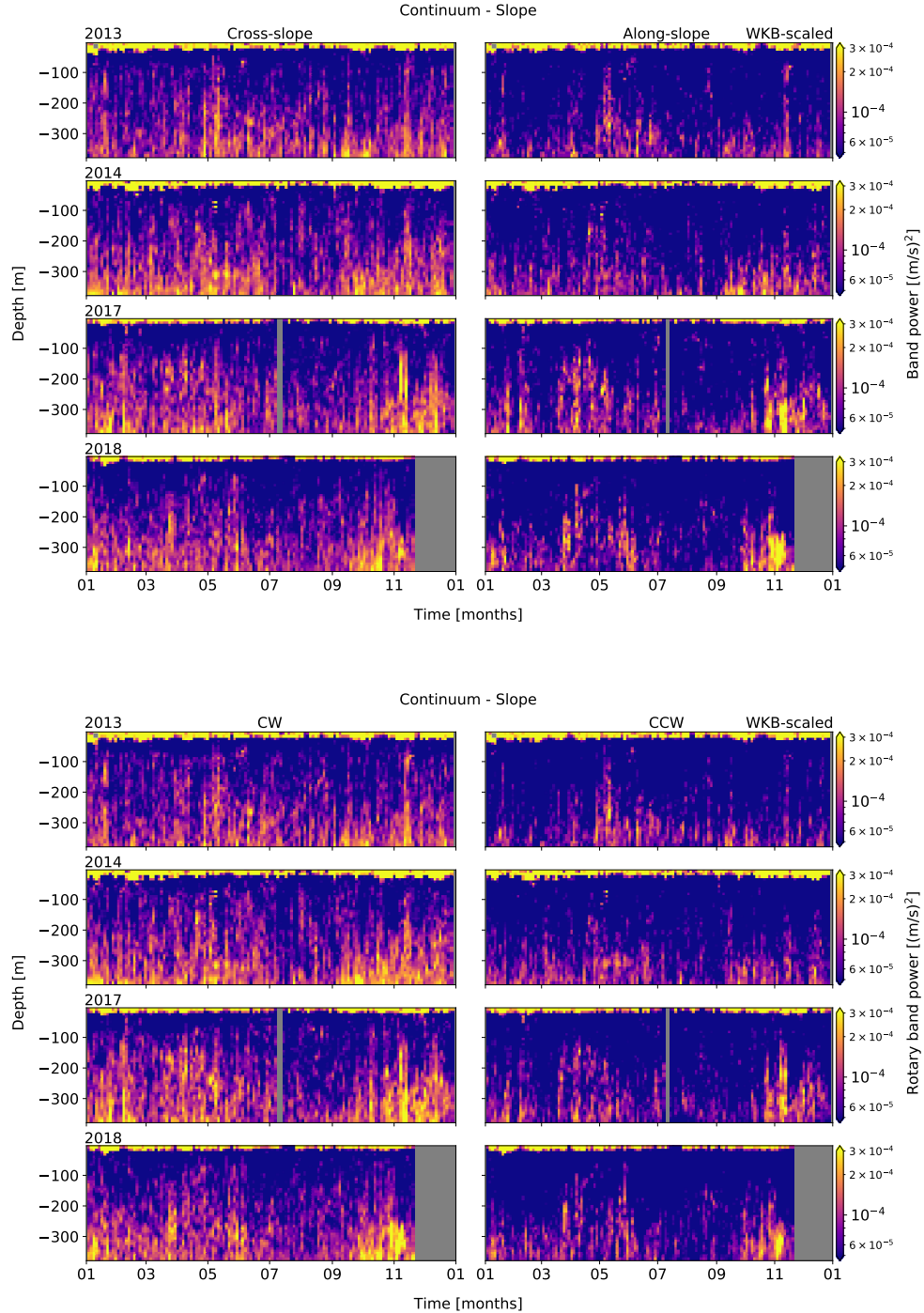


**Figure 21.** Band-integrated continuum PSD (upper) and rotary (lower) spectra for Slope, from WKB-scaled horizontal velocity data. Cross- (left) and along-slope (right) components are shown. Each row represents an analysis year, labelled at upper-left.

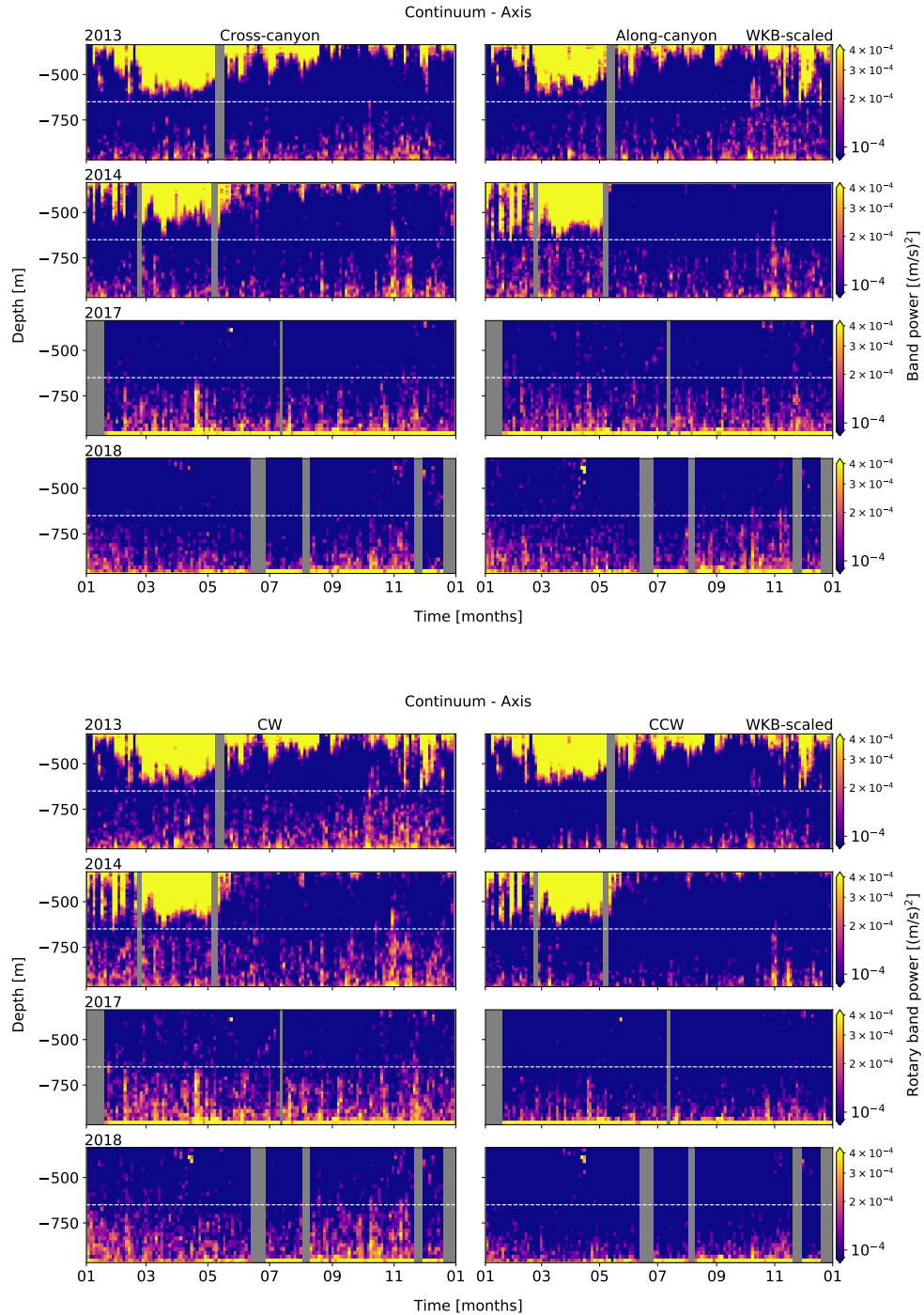


**Figure 22.** Band-integrated continuum PSD (upper) and rotary (lower) spectra for Axis, from WKB-scaled horizontal velocity data. Cross- (left) and along-slope (right) components are shown. Each row represents an analysis year, labelled at upper-left.

## 7 Discussion

### 7.1 Axis mean currents

The along-canyon mean flow at Axis is notable for IT seasonal and inter-annual consistency, as the defining feature of the lower canyon currents, and for implications regarding canyon interior circulation systems. At other sites, this circulation has been attributed to along-canyon pressure gradients due to large-scale exterior mean-currents, and turbidity currents or sediment underflow, and may indicate the presence of tidal rectification (Garrett, 2005; Xu and Noble, 2009; Chauvet et al., 2018)

To better characterise the currents, two-month snapshots of WKB-scaled low-pass velocities show the up-canyon flow is comprised of shoaling pulses with periodicity of about a week (Figure 23). Shoaling is consistent seasonally and inter-annually (not shown). Steady up-canyon propagation of periodic ( $>$  a few days) IW driven flow was noted in the lower depths of Hudson Canyon (Hotchiss and Wunsch, 1982), where shoaling was attributed to the sloped bottom and forcing associated with large-scale quasi-geostrophic flow cycles outside the canyon. In Monterey Canyon, Petruncio et al. (1998) also found shoreward IW driven flow that shoaled at an angle similar to that of the up-slope gradient, though periodicity was primarily semidiurnal.

To associate forcing for the observed periodicity, correlations were run for the Axis depth-mean time-series versus Slope mean-currents, spring-neap tidal cycles, and semidiurnal integrated spectral power. Results are entirely inconsistent (not shown), and do not suggest forcing from these sources. However, though there is no obvious link to diurnal or semidiurnal spring-neap forcing, estimates of total lower-canyon transport (below -680 m) from depth- and time-mean annual velocities result in near-zero net up-canyon flow (annually between 0.004 - 0.005 m/s), potentially consistent with tidal rectification theory (Garrett, 2005).

Though the along-canyon mean flow characteristics are similar to observations at other canyons, the periodicity and attributed forcing comparisons do not match. It is possible that such a circulation feature may be common in canyons, with unique forcing depending on the site. At Barkley Canyon, the along-canyon flow may be driven by a combination of physical processes beyond the scope of this paper, and warrants further research.

### 7.2 Tidal forcing

The diurnal and semidiurnal tidal constituents are two of the greatest sources of IW energy, and affect mean-currents and circulation on the VICS (Crawford

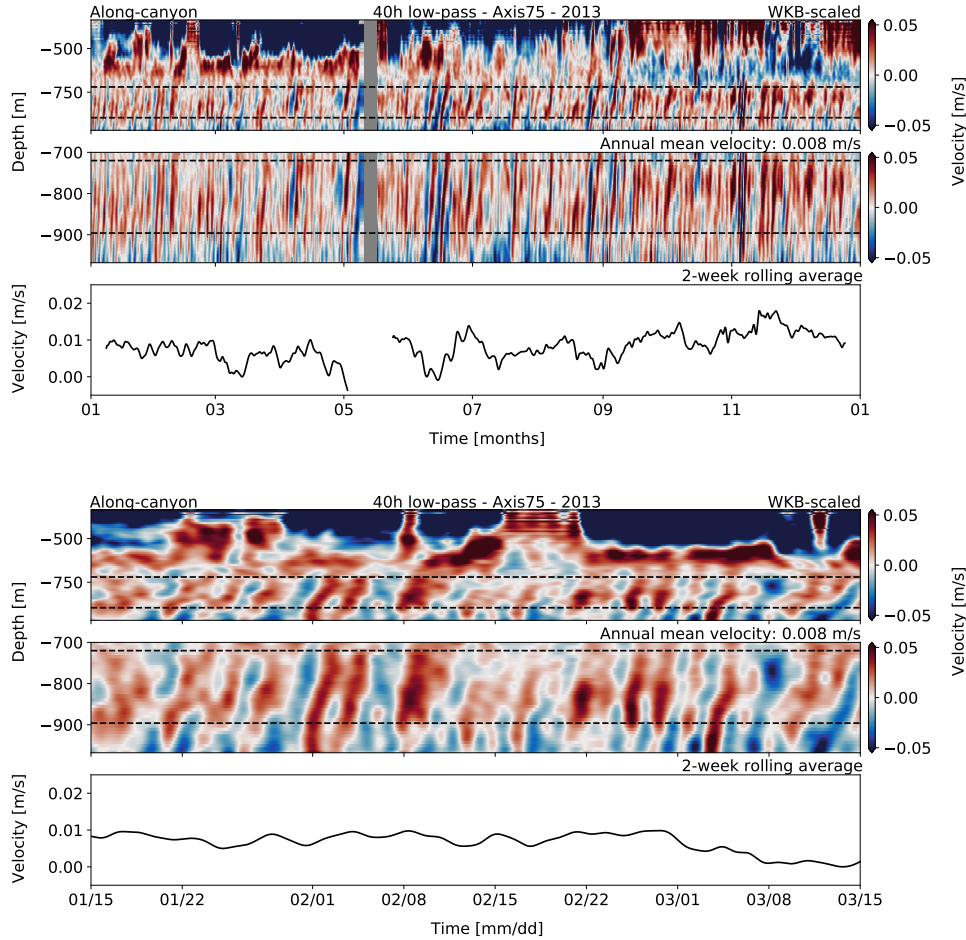


**Figure 23.** 40-hour low-pass WKB-scaled horizontal velocity data showing along-canyon mean-currents for Axis, annually (top) and in a two-month snapshot (bottom). Up-canyon flow is within the dashed lines; a thin near-bottom layer of down-canyon flow is below.

and Thomson, 1984). Barotropic and baroclinic tidal interaction with irregular topography can dissipate this energy, driving mixing and other high-frequency dissipative processes. An investigation of the diurnal and semidiurnal forcing at Barkley Canyon is important for understanding the seasonality of regional currents, baroclinic shelf-wave generation, and IT generation (Crawford and Thomson, 1984; Cummins and Oey, 1997).

Depth-mean diurnal power is consistently in-phase with the local barotropic diurnal spring-neap cycle, fortnightly and seasonally, with minimal phase-lag correlations and comparable seasonal amplitude (Figure 24). 3-month phase lag correlations were performed between the diurnal band-passed depth-mean

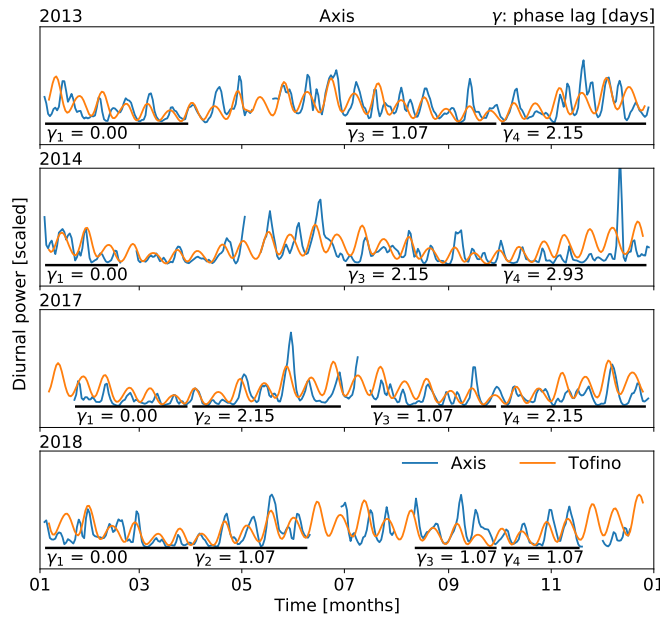
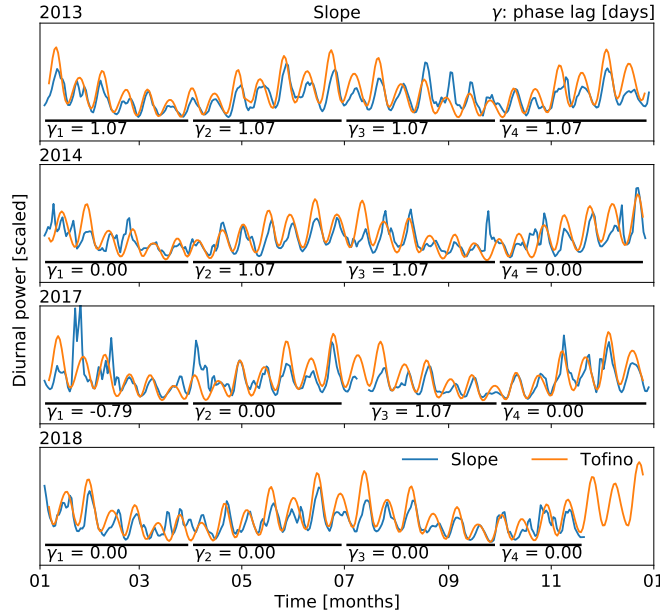


**Figure 24.** Diurnal barotropic forcing comparison. Phase-lag correlation and amplitude (scaled) comparisons for band-integrated power of diurnal surface level data (Tofino, orange) and WKB-scaled depth-mean diurnal power (blue) at Slope (top) and Axis (bottom). Black bars indicate seasonal correlation ranges. There is a consistent yet minor phase-lag, less than the time-scale of each spectral estimate.

power and nearby surface level time series, for months 1-3, 4-6, 7-9, and 10-12, each year. At Slope, the depth-mean was calculated beneath the surface side-lobe noise layer (below  $\sim -40$  m), and at Axis below and analysis depth limit of -680 m. As such, Axis estimates are only partial-depth and cannot fully resolve barotropic water-column motions. Surface-level data were obtained from the Canadian Hydrographic Service (CHS) operated gauge in Tofino, approximately 90 km due north of Barkley Canyon, as hourly time-series of deviation from chart datum. Surface level power spectra were diurnally band-passed using the same process as for observations, and site band-power interpolated to Tofino time-steps to compare phase. Phase-lag correlations range from null to about a day at Slope (multi-annual average of 0.5 days), and null to about two days at Axis (multi-annual average of 1.1 days) - both less than the time-resolution of the spectral estimates (2.7 days) used for the correlations. Comparing annual seasonality, the Tofino barotropic spring-neap amplitudes peak in months 6-8 and 11-2, corresponding well with the diurnal observations, consistent inter-annually.

If a diurnal phase-lag of about a day is present, as at Slope, this would suggest a baroclinic generation site within about 200 km - based on a  $K_1$  mode-1 wave speed of about 2 m/s (Crawford and Thomson, 1984). One candidate would be diurnal shelf waves generated by oscillatory tidal currents near the mouth of the Juan de Fuca Strait ( $\sim 100$  km east) that propagate poleward along the VICS (Flather, 1988). Confirmation of such waves would require additional instruments along the shelf, and is beyond the scope of this study. Other regions thought to be productive for baroclinic diurnal waves are either disconnected from the shelf (e.g. the abyssal Juan de Fuca Ridge) and cannot propagate sub-inertially to Barkley Canyon (Lavelle and Cannon, 2001), or too distant for the observed phase-lag (e.g. Mendocino Escarpment, 900 km south; Morozov, 2018). As there is enough uncertainty in the correlations that the phase-lag could be null, and considering the vertically linear structure, it seems likely that the diurnal band is primarily forced by the local barotropic spring-neap cycle, with possible seasonal contributions from shelf-waves, mean-current interactions, or stratification.

Semidiurnal barotropic spring-neap forcing is intermittently in-and-out of phase, at both sites (Figure 25). Phase-lag correlations were determined as for the diurnal band, with similar concerns regarding the Axis observations resolving a 'true' barotropic signal, due to IT partial depth-mean (below -680 m). Furthermore, as the scaled semidiurnal depth-mean band-power amplitudes vary greatly from the spring-neap levels, the accuracy of the phase-lag estimates is questionable. Results are inconsistent, and for 3-month periods range from

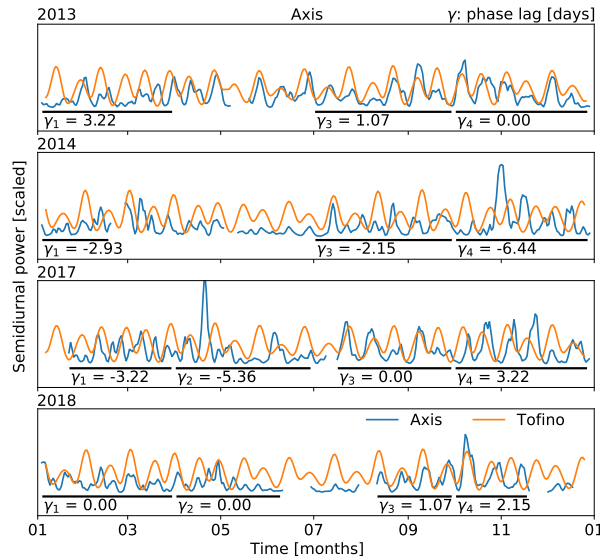
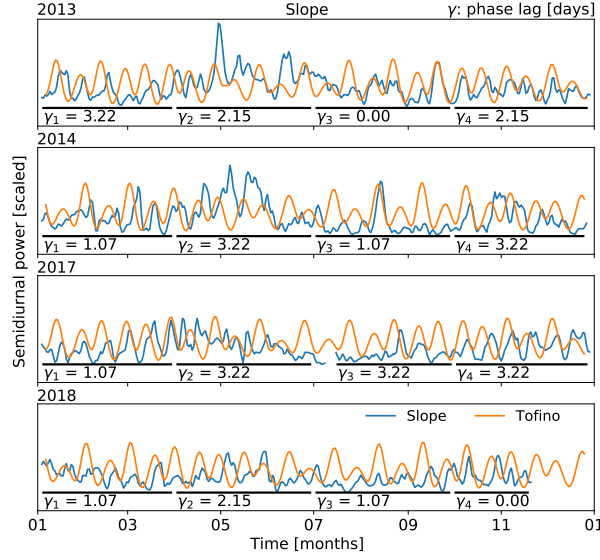


**Figure 25.** Semidiurnal barotropic forcing comparison. Phase and amplitude (scaled) comparisons for band-integrated power of semidiurnal surface level data (Tofino, orange) and WKB-scaled depth-mean semidiurnal power (blue) at Slope (top) and Axis (bottom). Black bars indicate seasonal correlation ranges. Though the instrument amplitude is highly irregular, there is a variable phase lag that suggests a mix of local barotropic and remote baroclinic forcing.

null up to about 4 days at Slope (multi-annual average of 2.3 days), and from

null up to about 6 days at Axis (multi-annual average of 2.8 days). For remote baroclinic forcing from up to four days away, as at Slope, a regional mode-1  $M_2$  phase speed,  $c_1 \sim 3.0$  m/s (Zhao et al., 2016) suggests a generation site of up to 1000 km. A likely origin is the Mendocino Escarpment running E-W off of Northern California, one of the strongest generation sites for low-mode semidiurnal IT in the northeast Pacific (Althaus et al., 2003; Arbic et al., 2012; Zhao, 2017; Morozov, 2018). Strong tide-topography generated northward propagating mode-1  $M_2$  IT, along with the escarpment's location about 800 km due south of Barkley Canyon ( $\sim 3.5$  days), agree reasonably with the observed phase lag. Other potential generation sites are closer (e.g. mouth of Juan de Fuca Strait  $\sim 100$  km, or Juan de Fuca Ridge  $\sim 400$  km) or are somewhat obstructed along their propagation paths (e.g. Haida Gwaii Islands, obstructed by northern Vancouver Island), but could still contribute.

Barkley Canyon is generally supercritical or near-critical to incident semidiurnal IT (Figure 4). Critical slope regions were determined from the gradient of bathymetry data obtained from the National Oceanic and Atmospheric Administration (NOAA) National Centre for Environmental Information, as 3 arc-second resolution mean sea level depth. At the Slope site, the local slope is  $\beta \approx 0.060$ , supercritical to the semidiurnal propagation angle  $\alpha_{M2} \approx 0.026$  at that depth, with a criticality ratio of 2.3 (Figure 6). This suggests downward reflection (CW) and focusing of incident semidiurnal IT. The Slope site sIT adjacent to a large near-critical region below the shelf-break (Figure 4), which, along with the VICS ITelf, is another source of observed downward semidiurnal energy (Drakopoulos and Marsden, 1993). For the Axis site on the canyon floor, the local slope angle is  $\beta \approx 0.019 < \alpha_{M2} \approx 0.036$ , with a criticality ratio of 0.53 (Figure 6). As such, this portion of the canyon floor is subcritical to semidiurnal IT, suggesting upward reflection. However, as the canyon walls are generally supercritical, and the surrounding floor is near-critical (Figure 4), the propagation of semidiurnal IT at Axis is likely complex. Xu and Noble (2009) found that deep in Monterey Canyon semidiurnal IT were not only scattered up-canyon along the subcritical floor from the mouth, but also reflected down by the supercritical walls, highly focusing semidiurnal energy near the bottom. The potential for scattering, reflection, focusing, and generation of semidiurnal IT at Axis could lead to highly 'channeled' deep-canyon semidiurnal motions.

The irregular nature of the spring-neap phase-lag suggests that the semidiurnal constituent is forced by a mix of local barotropic and remote baroclinic tides. As the barotropic tide passes over Barkley Canyon, near-critical slope topography generates and focuses semidiurnal IT, which radiate downward

from the shelf-break to the slope and canyon, where further downward reflection and focusing occurs. Remote IT are also subject to these effects, and alter observed seasonality based on their site of origin, likely Mendocino Escarpment to the south. Large-scale semidiurnal seasonal features may be contributed to by other factors, such as changes to stratification and mean-currents (Drakopoulos and Marsden, 1993; Cummins et al., 2000) - there is little annual seasonality in the semidiurnal spring-neap forcing to drive such inter-annual patterns.

### 7.3 Near-inertial forcing

NI forcing is qualitatively linked with regional wind events in the fall and early-winter (Figure 26), when NI energy is deposited into the surface ML, exciting internal NI currents that drive NI IW generation at the ML base (D'Asaro, 1995). It is interesting that NI band-power can be so strongly attenuated at Slope, while appearing simultaneously in the deep canyon, at Axis. To correlate regional wind forcing and the NI response at depth, wind data were obtained from the closest Fisheries and Oceans Canada (DFO) weather buoy, La Perouse (46206), approximately 50 km north of Barkley Canyon, as time series of magnitude and direction for each comparison year. The wind data has large data gaps during later analysis years (2014, 2017, 2018), so 2013 is used as the sample year for figures. Plots for other years are available in Appendix A (9).

A slab model analysis was conducted as in D'Asaro (1995) and Alford (2001), which gives a simplified idea of the ML response to NI forcing by the wind (Alford et al., 2016). Though simple, the model is continuously being improved to better account for non-homogeneous internal ML processes and ML to pycnocline energy transfer (Alford and Zhao, 2007; Jarosz et al., 2008; Alford et al., 2016; Zheng et al., 2017; Voelker, 2020; Alford, 2020). From the wind time series data, wind stress is calculated as in Garratt (1977), as:

$$\tau_0 = \rho C_D V(z)^2 \quad (12)$$

where  $\rho$  is the density of air approximated as 1,  $V(z)$  is the complex wind velocity vector, and  $C_D$  is the characteristic drag coefficient determined by:

$$C_D \times 10^3 = 0.51V^{0.46} \quad (13)$$

For appropriate seasonality, a mixed-layer of seasonally varying depth  $H$  must be considered, and is defined as by Thomson and Fine (2003) and Li et al. (2005) for the nearby (35 km) Line P station 3 (Figure 26). Assuming a null

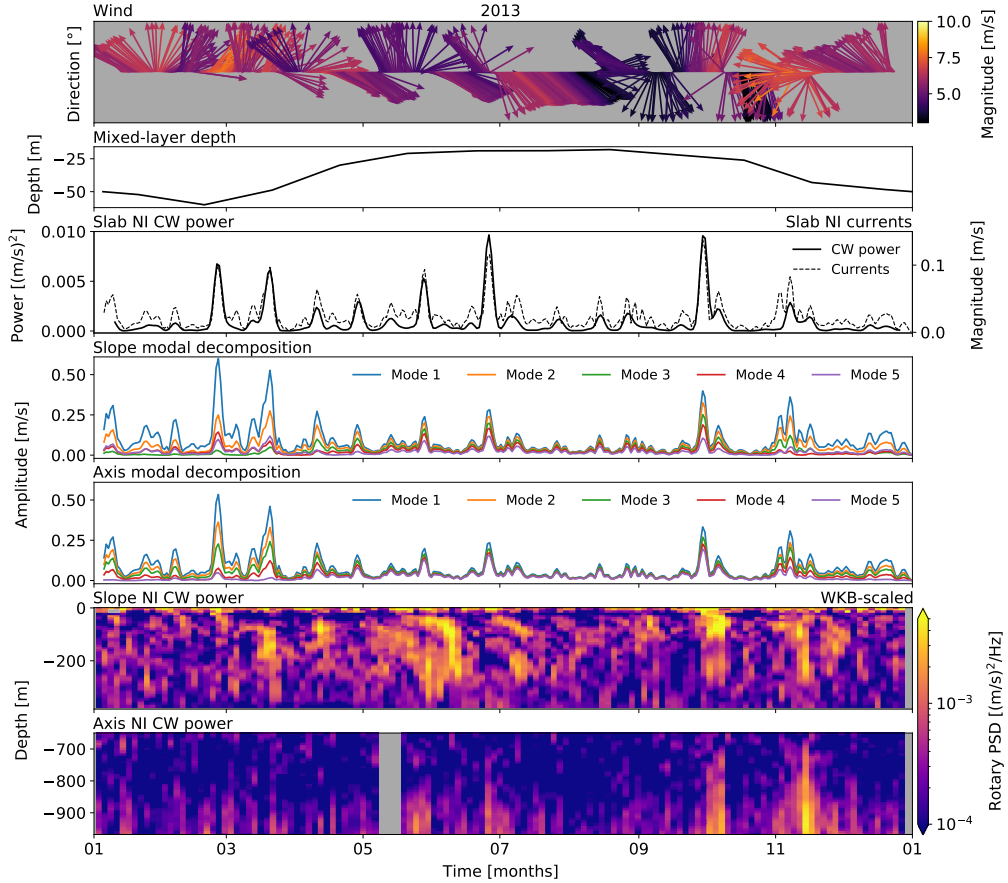


**Figure 26.** NI forcing analysis for 2013. Panels are (i) wind direction and amplitude, (ii) monthly-averaged ML depth for Line P station 3 as determined by Li et al. (2005), (iii) slab model NI CW power and NI currents, (iv, v) seasonal mode amplitudes for Slope and Axis, and (vi, vii) band-integrated NI CW power at Slope and Axis. There appears to be a complex relationship between the wind, ML, slab currents, and mode amplitudes in driving the NI observations, with the most obvious effects in the fall. Due to significant data gaps, plots for other analysis years are in Appendix A (9).

initialisation parameter  $u_{I1}$  at time  $t_1$ , wind generated slab layer currents at time  $t_2$  are then computed as:

$$u_{I2} = u_{I1} e^{-\omega \Delta t} - \frac{T_t}{H \omega^2} (1 - e^{-\omega \Delta t}) \quad (14)$$

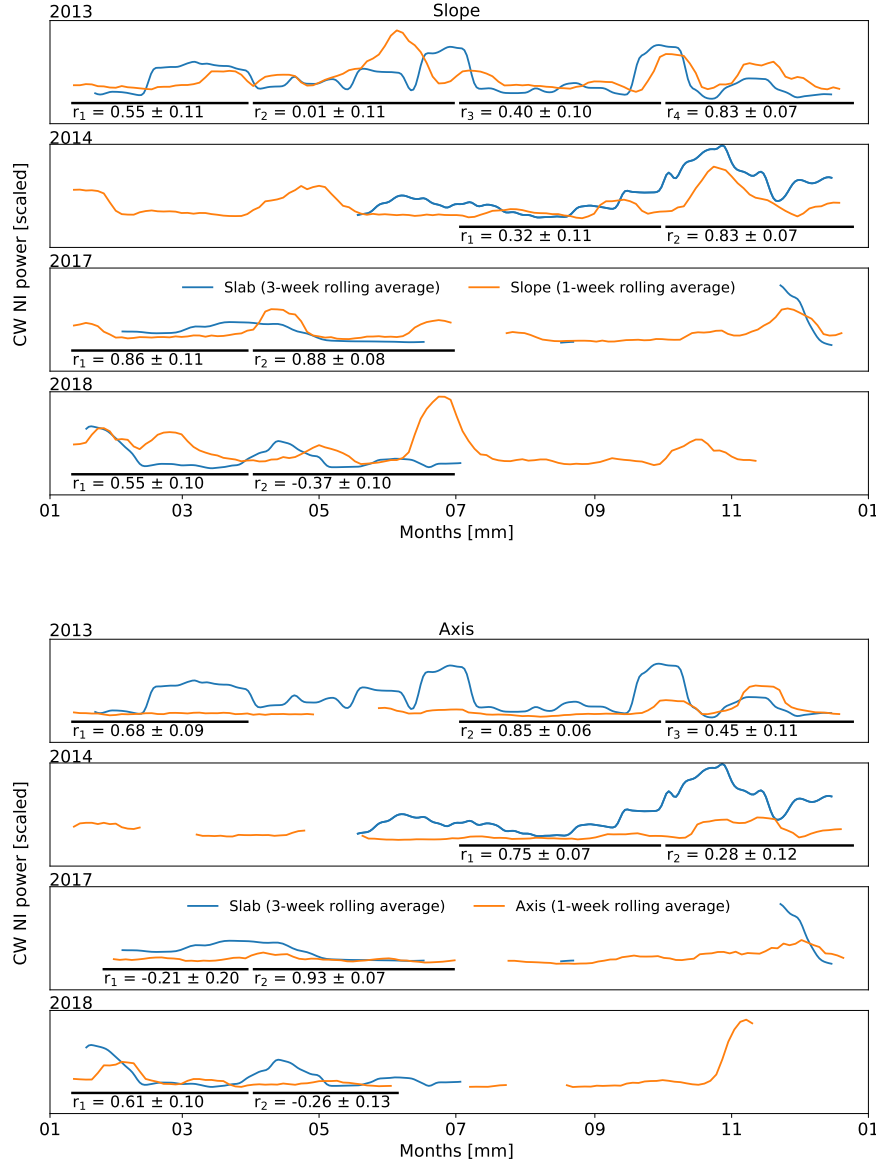


**Figure 27.** NI correlations. Seasonal Pearson correlation coefficients for scaled-amplitude comparisons of slab model CW NI power and Slope NI depth-mean band-power observations, at Slope (top) and Axis (bottom). Correlations are generally inconsistent, and are weak-positive in the fall, particularly at Slope.

where a damped rotation frequency,  $\omega$ , is determined as:

$$\omega = r + if \quad (15)$$

with  $r = 0.15f$  as an artificial damping parameter, as defined in Alford (2001);

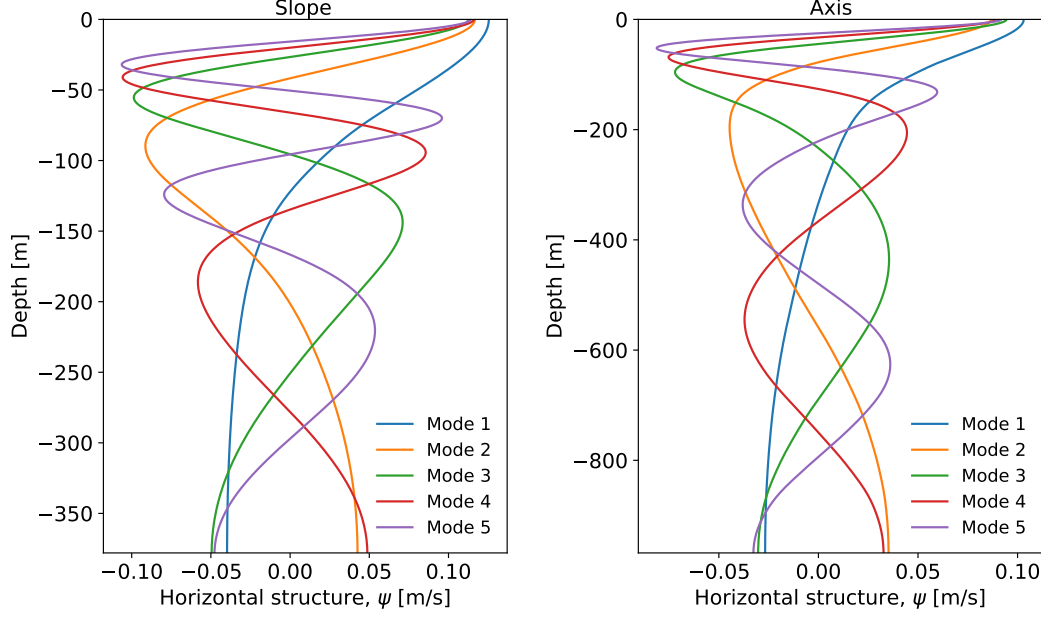


**Figure 28.** Vertical mode decomposition. Depth-dependent horizontal structure of mode amplitudes, for Slope (left) and Axis (right). Mode structure is dependent on site depth and the local stratification profile.

and

$$T_t = \frac{\Delta T}{\Delta t} \quad (16)$$

is related to the complex stress vector defined as:

$$T = \frac{\tau_x + i\tau_y}{\rho_{ML}} \quad (17)$$

where  $\rho_{ML} = 1024 \text{ kg/m}^3$  is the average density of the mixed-layer. The NI flux by the wind into the mixed layer at time  $t_2$  is then computed as:

$$\Pi = \text{Re} \left\{ \frac{T_t^*}{\Delta t |\omega|^2 H} \left[ \left( u_{I1} + \frac{T_t}{\omega^2 H} \right) (e^{-\omega \Delta t} - 1) + \frac{T_t}{\omega H} \Delta t \right] \right\} \quad (18)$$

. The slab currents are then band-passed for their NI component, resulting in  $u_{NI}$ .

Slab model results show intermittent NI mixed-layer currents associated with notable wind events (Figure 26). Slab currents,  $u_I$  (up to 0.5 m/s), and flux,  $\Pi$  (up to 0.25 m/s), induced by NI wind input (not shown) is comparable to what was found in previous studies by D'Asaro (1985), Alford (2001), and Voelker (2020). Band-passed NI ML currents are up to 0.1 m/s, and are visually

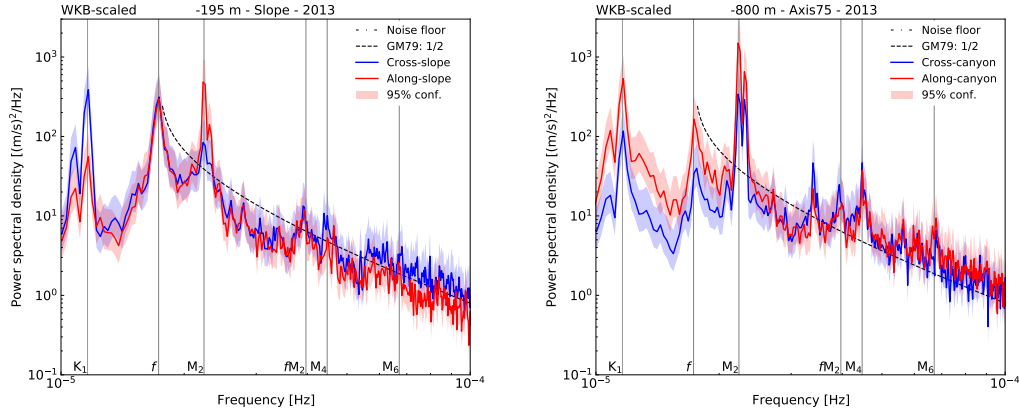


**Figure 29.** High frequency-resolution mid-depth PSD of WKB-scaled horizontal velocity data, for Slope (left) and Axis (right), in 2013. Frequency scale is zoomed to the tidal range. There are no additional peaks or apparent blue-shift for the NI constituent, suggesting local forcing.

linked with specific wind events, particularly when the ML is thin. As noted in Section 6.3.2, not every wind event contributes significantly to the ML NI response. Furthermore, not every event that shows up in the ML is evident in the observations. Seasonal Pearson correlation coefficients were obtained using a similar process as for the spring-neap correlations, for the slab CW NI power and depth-mean of NI band-power observations (Figure 27). The slab model may be considered overly simple to strongly correlate ML NI currents with site observations (Alford et al., 2016), so a rolling average was applied to each time-series and relaxed until correlations began to devolve. Ideal rolling averages were found to be 3-weeks for the slab data, and 1-week for site observations. At Slope, correlations are strong-positive in the fall, and weak- to medium-positive in summer. At Axis, in 2013 and 2014 correlations are strong-positive in summer, and weak- to medium-positive in fall. Correlations are otherwise inconsistent. The fall and summer correlation periods encompass notable wind events that occur while the ML is still thin, and when there appears to be a greater response at depth. Furthermore, there is an apparent lag in the observation time-series that may be related to the noted propagation of NI energy from the ML to pycnocline, affecting statistical correlation with the quick slab response.

For NI IW generation by the NI ML currents, the stratification-dependent vertical mode structure is determined from the solutions of the Sturm-Liouville equation (Alford and Zhao, 2007), as in Section 3). The solutions provide the vertical structure of each mode, and seasonal NI mode amplitudes can then

be found using ML depth as a time-dependent step-function for convolution with the ML NI currents.

Vertical mode decomposition shows that high-mode contribution may lead to greater NI response, at depth (Figures 26 and 28). The ML is thick in winter and spring (down to about -60 m), and thinnest summer through early-fall (up to about -20 m). At both sites, when the ML is thin, contributions from low modes (1 and 2) and high modes (3, 4, 5) are about equal ( $\sim 52\%$  low modes); when the ML is thick, modes 1 and 2 dominate ( $\sim 74\%$ ). Similar to the slab response, at both sites there is a greater NI response when the ML is thin and higher modes are equal contributors. The early-fall is the most responsive, when there are strong wind events, the ML is still thin, and high modes are prevalent. High modes contribute most in the summer, when the ML is thinnest and there are few storms, yet even weak summer wind events can warrant a response in the interior, including the deep canyon. In contrast, there are many strong wind events in winter and spring, but the ML is thick, low modes dominate, and the interior does not respond. Seasonal mode-1 amplitudes of up to 0.6 m/s occur after notable wind events, similar to findings by Jarosz et al. (2007) at DeSoto Canyon, who found that low modes generally dominate but most NI activity is observed when the ML is thin. Alford et al. (2016) note that it is high mode waves that propagate downward, while low mode waves contribute more to horizontal motions.

Results suggest that NI forcing at the surface is complex, dependent on variable characteristics of both wind events and ML processes, leading to highly intermittent seasonality. Remote forcing is also possible, as free high-mode NI IW generated at the base of the surface mixed-layer must propagate equatorward due to the effects of turning latitudes (Alford et al., 2016). There is often a blue-shift associated with remote NI forcing (Garratt, 1977; Voelker et al., 2020); however, high frequency-resolution spectra (Figure 29) do not resolve any additional NI peaks, with a single peak situated at the local inertial frequency ( $1.73 \times 10^{-5}$  Hz). Forcing may be further complicated by the weather buoy location 50 km north, or trapping of NI energy by mesoscale circulation (Alford et al., 2016). Regardless, strong qualitative and moderate quantitative correlations suggest that NI observations are most responsive to notable wind events during periods of thin ML depth and increased high-mode contributions, particularly in the late-summer and fall, and consistent inter-annually. Potential alternative forcing for deep NI flow in the canyon could be from mean-currents or lee waves of NI frequency across the mouth or rim of the canyon, where attenuation effects may be reduced, with such investigation beyond the scope of this study.

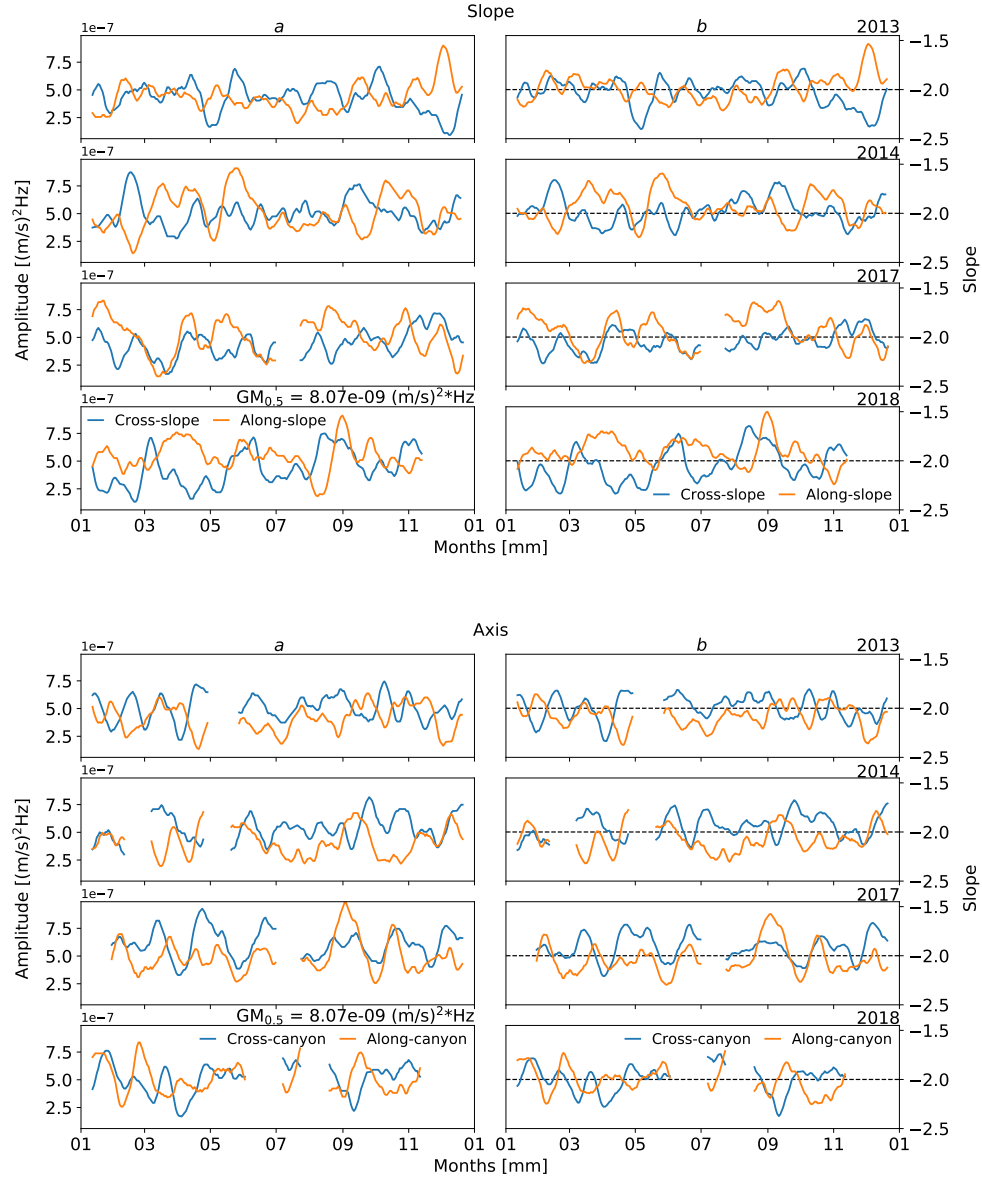


**Figure 30.** Time-series of continuum power law fit. Continuum amplitude, *a* (left), and slope, *b* (right), of power law ( $a f^b$ ) fit to lower-depth WKB-scaled PSD, at Slope (top) and Axis (bottom). Compared to GM, amplitudes are elevated in the enhancement layer, while slope can vary around -2.

## 7.4 Continuum analysis

As continuum seasonality is linked to a cascade of IW energy from low-frequency (tidal and sub-tidal) to high-frequency (continuum) dissipative pro-

cesses (Polzin, 2004), topographic enhancement of the lower frequency constituents can indicate elevated mixing at Barkley Canyon. To evaluate the state of the IW continuum, a comparison with the canonical open-ocean GM IW spectrum can provide information on energy distribution and dissipative effects in the local IW field.

At depth, the amplitude of the continuum is higher than for GM, while the slope is similar (Figure 30). For each component-wise window of the high frequency-resolution WKB-scaled PSD estimates (2048 point Hanning window, 50% overlap) a power law of  $af^b$  was fit to the continuum range ( $7 \times 10^{-5} - 1.2 \times 10^{-4}$  Hz) for time series of  $a$  and  $b$ , for lower-depths at Slope (-299 m) and Axis (-880 m). A 2-week rolling average was then applied. Each power bin of the open-ocean GM continuum range was 'whitened' - multiplied by its corresponding frequency value, squared - and an average value determined for  $GM_{0.5} = 8.07 \times 10^{-9} (\text{m/s})^2 \text{Hz}$ . At both sites, amplitudes are fairly steady, ranging within  $10^{-7} (\text{m/s})^2 \text{Hz}$ ,  $\sim 2 \times$  orders of magnitude higher than GM.  $b$  values are also fairly steady, ranging from about -1.6 – -2.4, near the GM value of -2. Matching components for amplitude and slope are of similar shape, rough copies of the seasonal variability of continuum depth-band power, and appear to increase/decrease together.

Depth-dependent continuum amplitudes are greater than the open-ocean GM spectrum, near topography (Figure 31). To better inspect the effects of topography on continuum amplitudes, each power bin of WKB-scaled continuum band-power was 'whitened', and an average value determined as  $c$ . These were compared at each time and depth versus  $GM_{0.5}$ . Results show  $c$  amplitudes up to  $7 \times$  GM at both sites, at times and depths coinciding with observed continuum band-power pulses. This seasonality is identical to that of continuum band-power. Furthermore, the differences in component amplitudes suggest that the near-topography continuum is characteristically non-GM-like (GM being isotropic).

Elevated near-topography continuum amplitudes lead to enhanced dissipation rates,  $\varepsilon$ , at both sites (Figure 32). From IW interaction theory (Althaus et al., 2003), dissipation estimates were calculated from the WKB-scaled  $c$  amplitudes as:

$$\varepsilon = \varepsilon_0 \frac{N^2}{N_0^2} \frac{\langle V_z^2 \rangle^2}{\langle GM V_z^2 \rangle^2} f(R_\omega) \quad (19)$$

where  $\varepsilon_0 = 4.1 \times 10^{-11} \text{ W/kg}$ ,  $N_0 = 5.24 \times 10^{-3} \text{ rad/s}$  is the GM reference buoyancy frequency,  $N = 2.53 \times 10^{-3} \text{ rad/s}$  is the local reference buoyancy frequency used for WKB scaling,  $\langle V_z^2 \rangle^2 / \langle GM V_z^2 \rangle^2$  is the measured shear/strain ratio of continuum energy versus GM energy over the same bandwidth, and

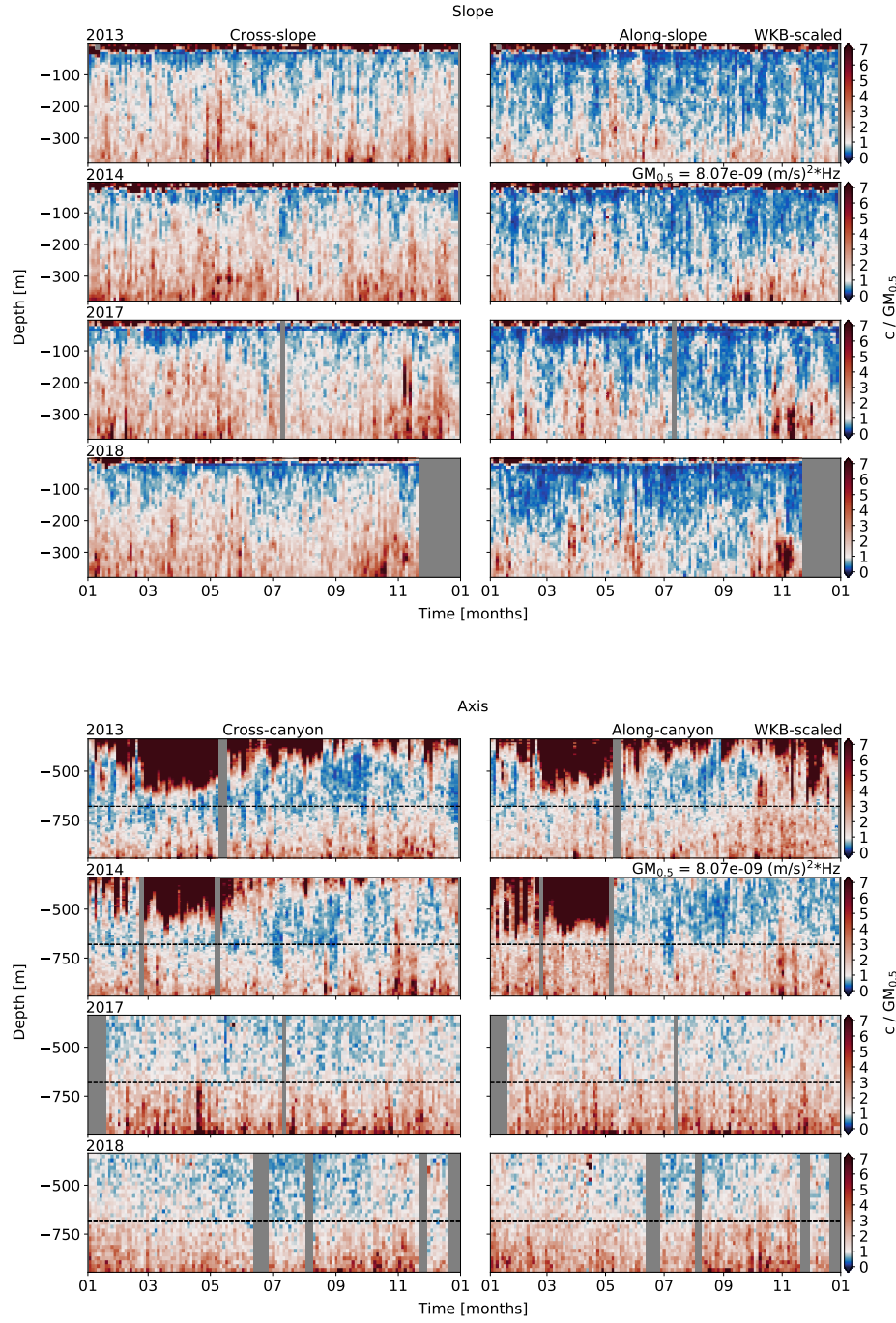


**Figure 31.** Continuum amplitude ( $c$ ) versus component-wise GM amplitude, for Slope (top) and Axis (bottom). Results are obtained from WKB-scaled spectra of horizontal velocity data. Continuum amplitudes are generally enhanced near topography, as compared to the open-ocean GM spectrum.

the upper bound:

$$f(R_\omega) = \left(\frac{R_\omega + 1}{R_\omega}\right)^2 \left[ \text{arc cosh}\left(\frac{N}{f}\right) + \frac{25\text{arc cos}(f/N)}{\sqrt{R_\omega}} \right] \quad (20)$$

is as defined by Sun and Kunze (1999), with  $R_\omega = 2.13$  being the semidiurnal shear/strain ratio used by Kunze et al. (2002). Results are consistent with those found in other slope and canyon regions, exceeding  $10^{-8}$  W/kg near topography at both sites (Kunze et al., 2002), with seasonality corresponding to continuum band-power and c/GM ratios.

Turbulent eddy diffusivities,  $\kappa$ , are similarly elevated near topography (Figure 32). Using the dissipation rates determined from WKB-scaled  $c$  values, diffusivity was calculated as by Kunze et al. (2002) as:

$$\kappa = \frac{\gamma\varepsilon}{N^2} \quad (21)$$

where  $\gamma = 0.2$  is the mixing efficiency for high-Reynolds-number turbulence. Turbulent eddy diffusivities are again similar to findings at other slope and canyon sites, exceeding  $10^{-4}$  m<sup>2</sup>/s near topography (Kunze et al., 2002). Seasonality is again linked to continuum band-power, c/GM ratios, and dissipation rates. In open water beyond the enhancement layer, diffusivity values are at least an order of magnitude less than  $10^{-5}$  m<sup>2</sup>/s, consistent with values found in open-ocean regions (Kunze et al., 2002).

Continuum seasonality is correlated with semidiurnal forcing at both sites, as well as the sub-diurnal band at Slope, and the NI band at Axis (Figures 33 and 34). Seasonal Pearson correlation coefficients were determined for the depth-mean of continuum band-power versus the depth-mean of each other frequency band. As for the NI slab model response, a rolling average was relaxed until correlations began to devolve, settling at a 2-week window. At Slope, the semidiurnal band shows moderate- to strong-positive correlations in the spring, when it experiences a pulse associated with seasonally dependent stratification (Drakopoulos and Marsden, 1993). The sub-diurnal band shows weak- to moderate-positive correlations in both the winter and spring. At Axis, the semidiurnal band is strong-positive at all times of year, while the NI band is moderate- to strong-positive in the spring and fall. There is no fortnightly or annual modulation of continuum power or vertical scale associated with diurnal or semidiurnal spring-neap effects, yet the semidiurnal band is a clear contributor to continuum seasonality.

Speculatively, topographic focusing of low-frequency (sub-tidal and tidal) IW enhances the cascade of energy to high-frequency (continuum) dissipative processes, elevating the continuum amplitude and driving mixing. At Slope, the

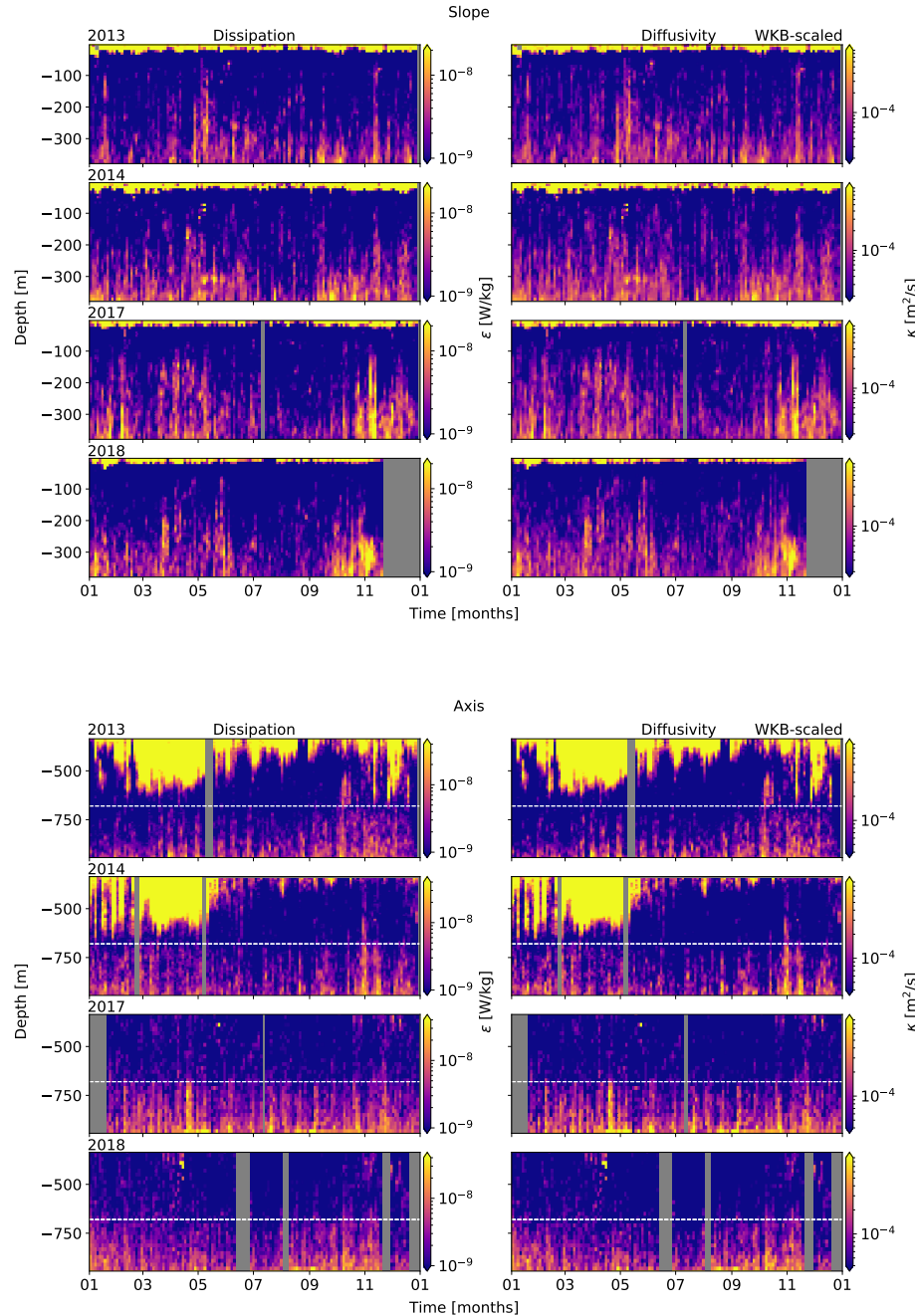


**Figure 32.** Dissipation rates (left) and turbulent eddy diffusivity (right), for WKB-scaled horizontal velocity spectra at Slope (top) and Axis (bottom). Both dissipation and diffusivity are heightened near topography.

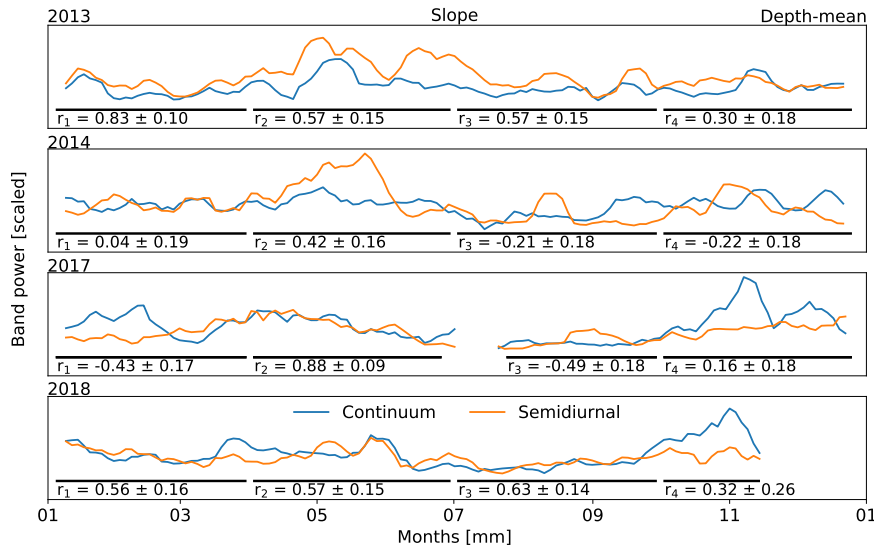
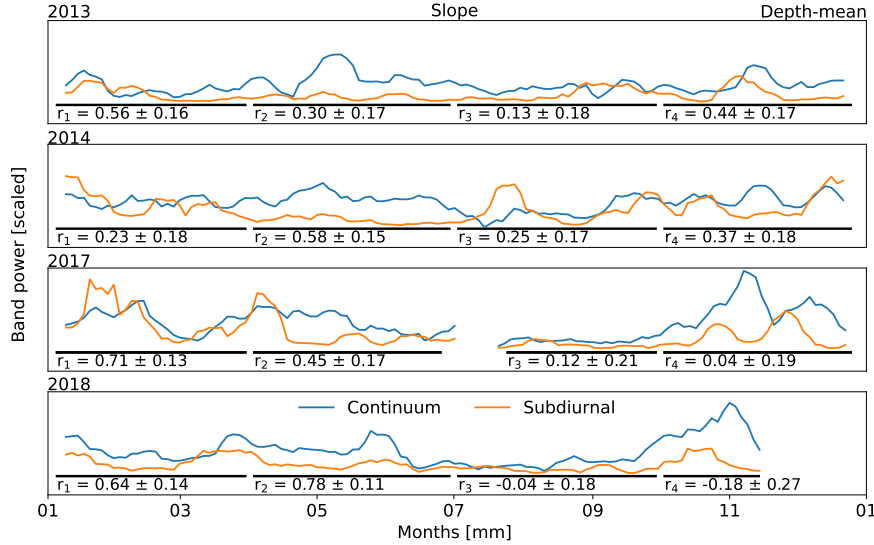


**Figure 33.** Seasonal (3-month) Pearson correlation coefficients for depth-mean band-power of the continuum versus the sub-diurnal (top) and semidiurnal (bottom) bands, at Slope. A 2-week rolling average has been applied to the time-series. Both bands show some correlation with the continuum in the winter and spring, but correlations are inconsistent in the latter half of each year.

most powerful frequency constituents are the sub-diurnal currents and the near-critical semidiurnal IT, particularly in spring. At Axis, sub-diurnal currents are weakened and the focused semidiurnal IT dominate throughout the

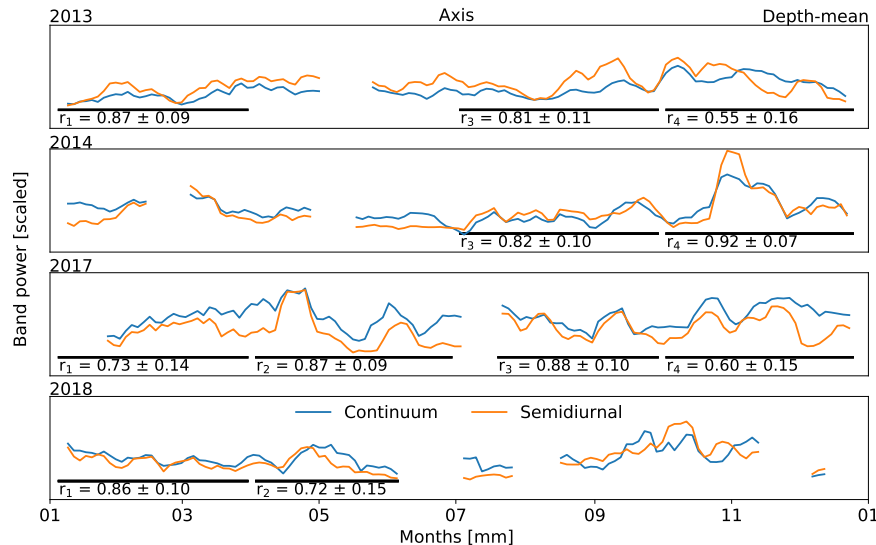
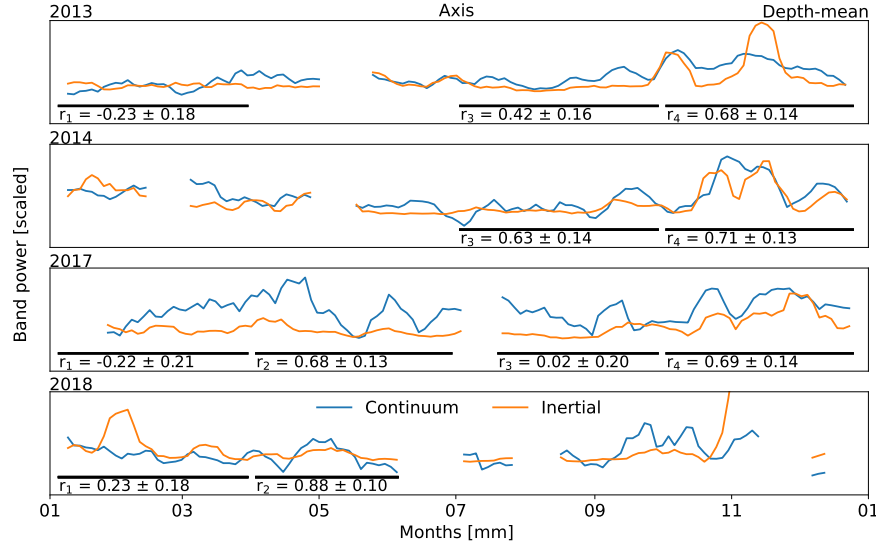


**Figure 34.** Seasonal (3-month) Pearson correlation coefficients for depth-mean band-power of the continuum versus the NI (top) and semidiurnal (bottom) bands, at Axis. A 2-week rolling average has been applied to the time-series. The semidiurnal band shows moderate- to strong-positive correlations throughout the year, while the NI band shows generally moderate-positive correlations (except winter).

year, though the occasional NI pulse makes it into the canyon in fall. These bands likely contribute the most energy to high-frequency dissipative topographic interactions, driving the observed continuum seasonality that is con-

sistent inter-annually. However, there are likely additional contributions from other bands, and unknown effects due to physical processes beyond the scope of this study.

## 8 Summary and conclusions

It was found that there is significant influence from topography on the local IW field at both sites, guiding flow (with consistent up-canyon currents above a thin down-canyon layer) and causing frequency-dependent focusing (or attenuation, for NI at Slope) of spectral power, generally up to  $1.5\times$  orders of magnitude 150 m AB at Slope, and up to  $2\times$  orders of magnitude 250 m AB at Axis. There is little inter-annual variability. The near-topography enhancement has unique seasonality for individual frequency constituents that varies little inter-annually. Sub-diurnal and diurnal flows are sub-inertially trapped along topography, and the diurnal band appears to be forced locally (barotropically). Free semidiurnal IT are focused and reflected near critical topography, and appear to experience both local and remote (baroclinic) forcing. The NI band is attenuated near the slope, yet enhanced near the canyon bottom, with intermittent forcing that appears linked to regional wind events, high-mode propagation, and the seasonal ML depth. The state of the IW continuum is elevated as compared to the open-ocean GM spectrum (up to  $7\times$  GM), with enhanced dissipation (exceeding  $10^{-8}$  W/kg) and diffusivity (exceeding  $10^{-4}$  m<sup>2</sup>/s) near topography, and seasonality correlations suggesting a cascade of energy from low-frequency constituents (primarily semidiurnal, with contributions from the sub-diurnal at Slope, and NI at Axis) to high-frequency dissipative processes.

Unfortunately, the WKB-stretch scaling applied throughout much of the analysis is based on deep CTD casts that were made nearby (21 km SE), but away from topography; the stratification profile captures the surface ML and pycnocline, but does not account for stratification adjustment near the slope or in the canyon (Figure 7). Hotchkiss and Wunsch (1982) noted increased stratification near areas of high 'topographic relief', such as the shelf-break and slopes. These highly stratified turbulent layers experience the effects of reflection, scattering, and IT and lee-wave generation, as well as amplification of IW and IT. To properly mitigate the effects of depth dependent stratification variability, further research would benefit from site specific climatology data.

Results could also be improved through increased sampling consistency between instruments (there were maintenance periods and instrument redeploy-

ments during analysis years), additional instrument sites (along the canyon floor and rim), and additional overlapping comparison years between sites. Broader temporal coverage could provide insight into decadal seasonality, while spatial expansion would allow for observations of along-topography IW propagation. This study was not able to identify forcing for the periodicity of the shoaling up-canyon mean-currents at Axis, the sub-diurnal range's intermittent seasonality, or accurately identify sites of origin for incident baroclinic IT.

Barkley Canyon is a dynamic submarine canyon and slope region with physical processes that are heavily influenced by topography. Currents, tides, and wind all contribute to an energetic region of IW and IT, driving mixing and other dissipative processes. As canyons and slopes are known as hot-spots for IW driven mixing, contributing significantly to regional transport of energy, shelf productivity, and even large-scale ocean circulation and climate effects, ONC's NEPTUNE cabled observatory is an important network for further investigation of the VICS, and beyond. Due to the accessibility of publicly available data, Barkley Canyon is a key observational laboratory for not only furthering ocean research, but fostering collaboration between members of the amateur and professional scientific communities. It is hoped that this study has provided insight leading to such research and collaboration, as well as a better understanding of the importance of shelf-incising canyons as fundamental to physical ocean processes.

## 9 Appendix A: Supplemental plots

### 9.1 Wind comparisons

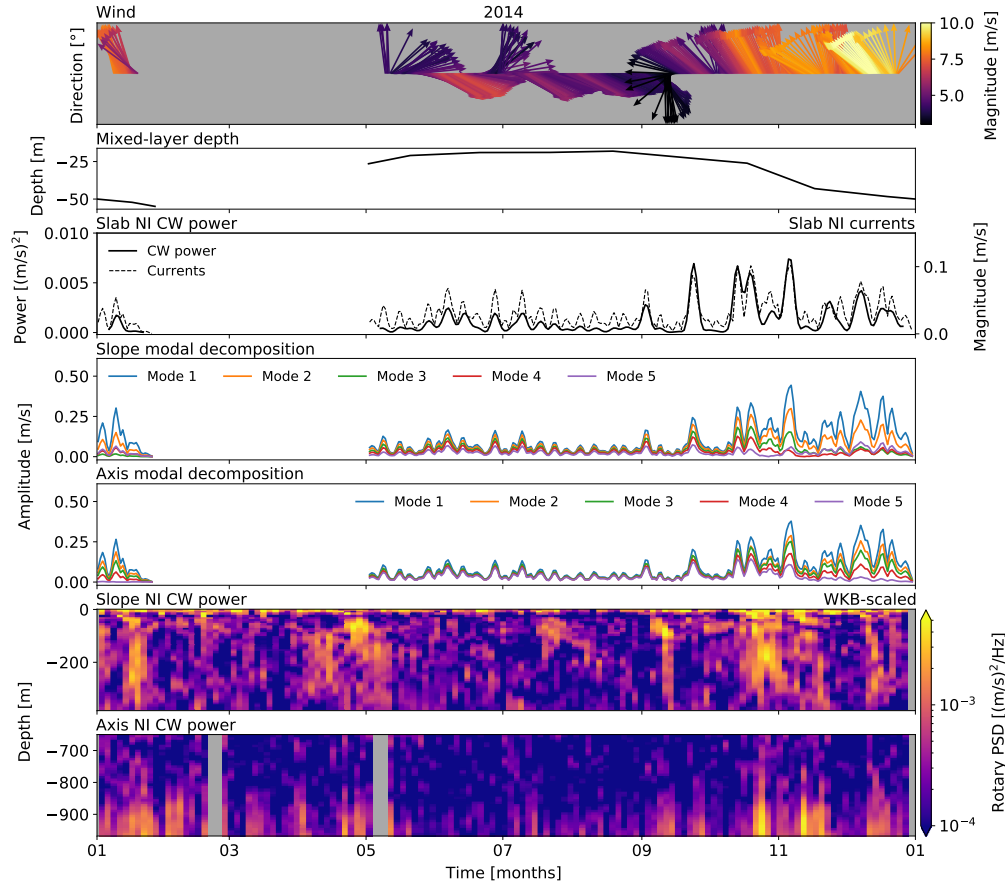


**Figure 35.** NI forcing analysis for 2014. Panels are (i) wind direction and amplitude, (ii) monthly-averaged ML depth for Line P station 3 as determined by Li et al. (2005), (iii) slab model NI CW power and NI currents, (iv, v) seasonal mode amplitudes for Slope and Axis, and (vi, vii) band-integrated NI CW power at Slope and Axis. There appears to be a complex relationship between the wind, ML, slab currents, and mode amplitudes in driving the NI observations, with the most obvious effects in the fall.

### 9.2 Continuum correlations

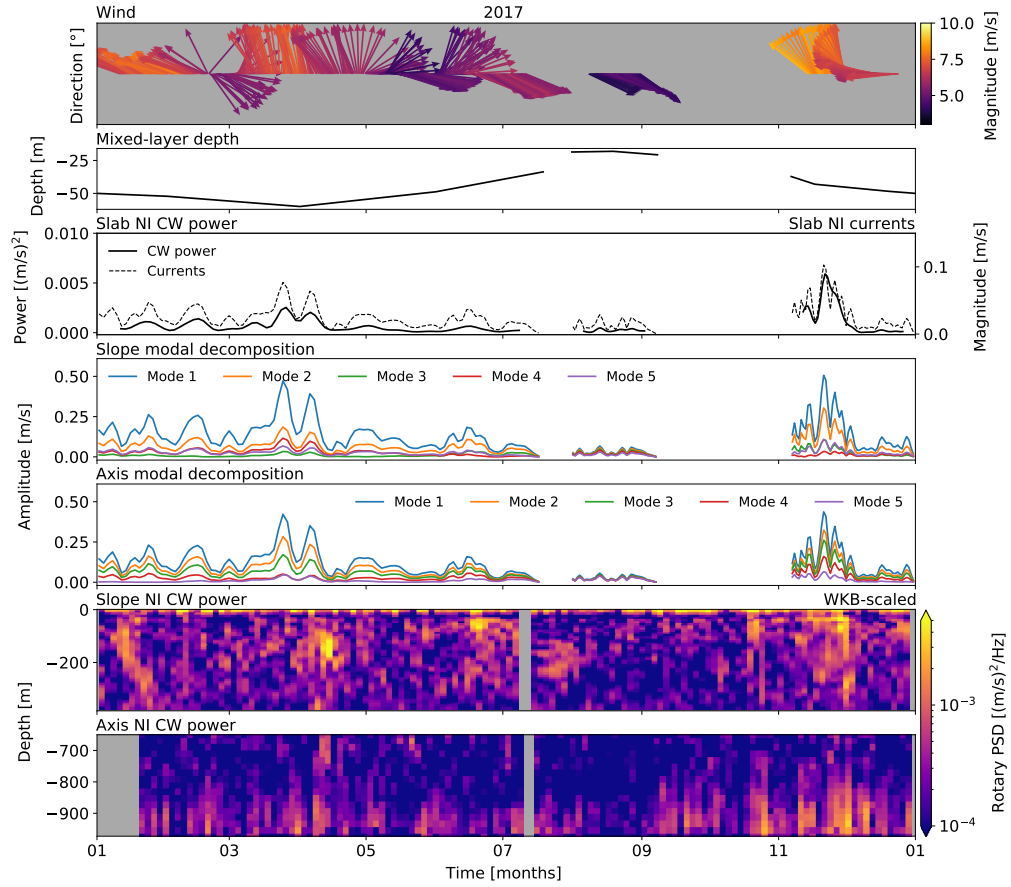


**Figure 36.** NI forcing analysis for 2017. Panels are (i) wind direction and amplitude, (ii) monthly-averaged ML depth for Line P station 3 as determined by Li et al. (2005), (iii) slab model NI CW power and NI currents, (iv, v) seasonal mode amplitudes for Slope and Axis, and (vi, vii) band-integrated NI CW power at Slope and Axis. There appears to be a complex relationship between the wind, ML, slab currents, and mode amplitudes in driving the NI observations, with the most obvious effects in the fall.

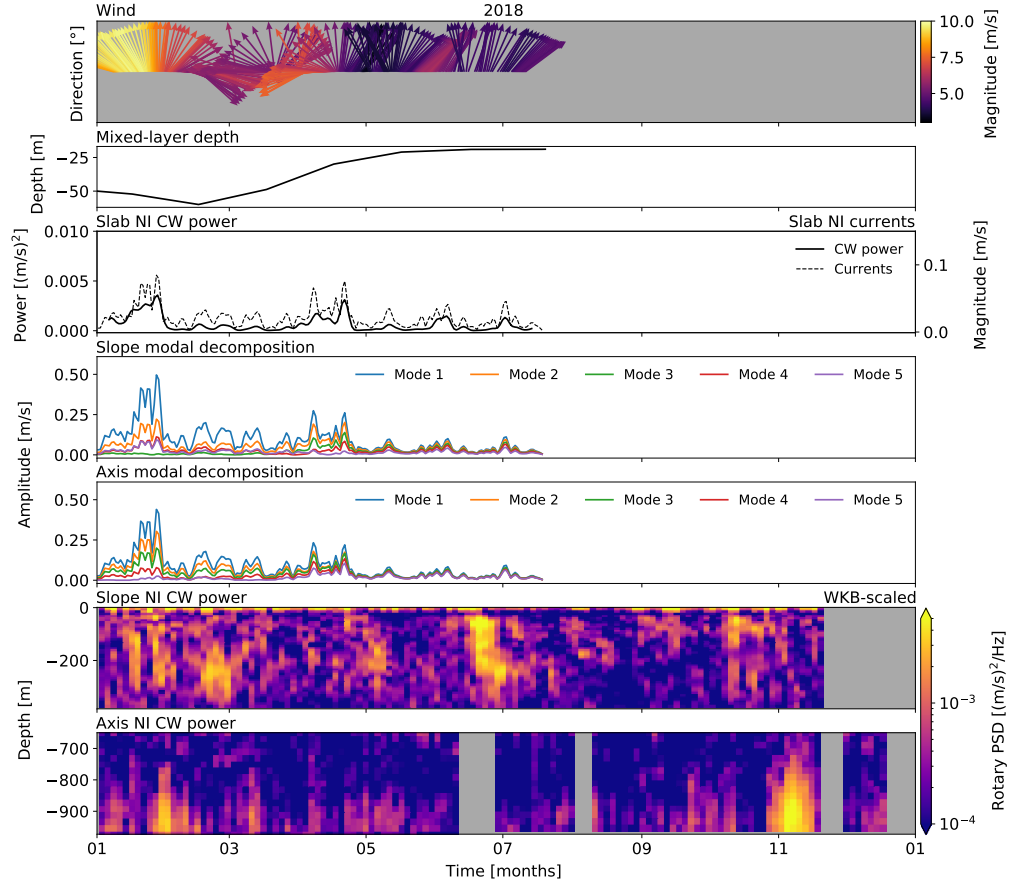


**Figure 37.** NI forcing analysis for 2018. Panels are (i) wind direction and amplitude, (ii) monthly-averaged ML depth for Line P station 3 as determined by Li et al. (2005), (iii) slab model NI CW power and NI currents, (iv, v) seasonal mode amplitudes for Slope and Axis, and (vi, vii) band-integrated NI CW power at Slope and Axis. There appears to be a complex relationship between the wind, ML, slab currents, and mode amplitudes in driving the NI observations, with the most obvious effects in the fall.

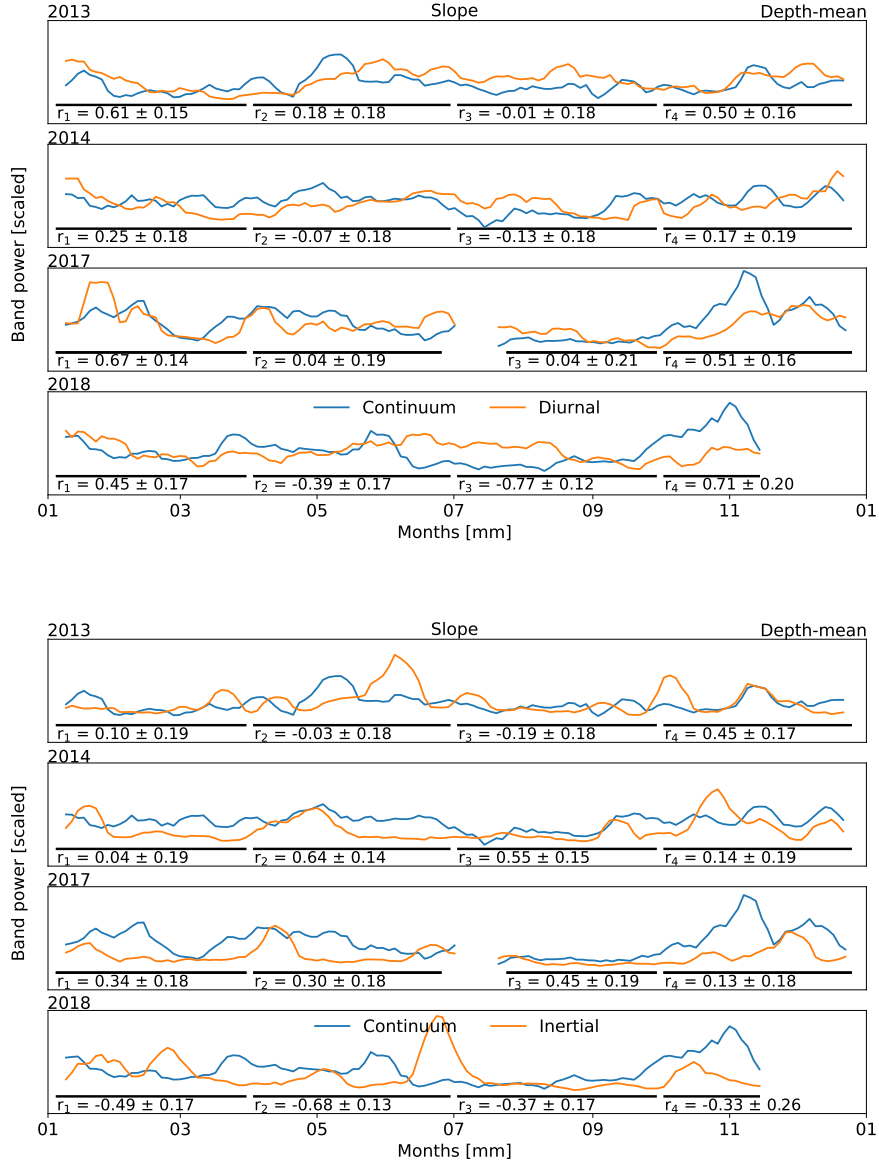


**Figure 38.** Seasonal (3-month) Pearson correlation coefficients for depth-mean band-power of the continuum versus the diurnal (top) and inertial (bottom) bands, at Slope. A 2-week rolling average has been applied to the time-series. Both bands show some correlation with the continuum in the winter and spring, but correlations are inconsistent in the latter half of each year.

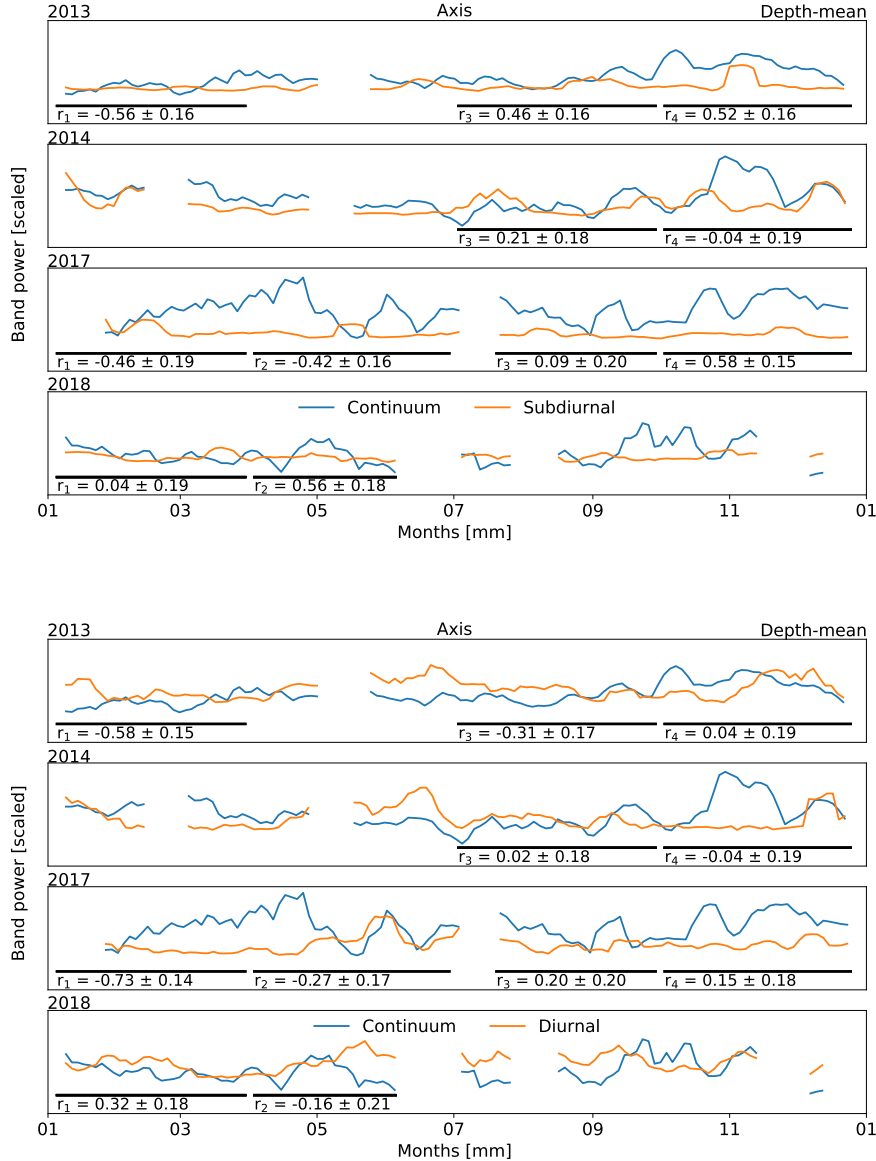


**Figure 39.** Seasonal (3-month) Pearson correlation coefficients for depth-mean band-power of the continuum versus the sub-diurnal (top) and diurnal (bottom) bands, at Slope. A 2-week rolling average has been applied to the time-series. Both bands show some correlation with the continuum in the winter and spring, but correlations are inconsistent in the latter half of each year.

## 10 References

*Incomplete*

- Alford, M. H., MacKinnon, J. A., Zhao, Z., Pinkel, R., Klymak, J., & Peacock, T. (2007). Internal waves across the Pacific. *Geophysical Research Letters*, 34(24), 24601. <https://doi.org/10.1029/2007GL031566>
- Alford, M. H., Cronin, M. F., & Klymak, J. M. (2012). Annual cycle and depth penetration of wind-generated near-inertial internal waves at ocean station papa in the northeast pacific. *Journal of Physical Oceanography*, 42(6), 889–909. <https://doi.org/10.1175/JPO-D-11-092.1>
- Allen, S. E., Vindeirinho, C., Thomson, R. E., Foreman, M. G. G., & Mackas, D. L. (2001). Physical and biological processes over a submarine canyon during an upwelling event. *Canadian Journal of Fisheries and Aquatic Sciences*, 58(4), 671–684. <https://doi.org/10.1139/f01-008>
- Carter, G. S., & Gregg, M. C. (2002). Intense, variable mixing near the head of Monterey Submarine Canyon. In *Journal of Physical Oceanography* (Vol. 32). [https://doi.org/10.1175/1520-0485\(2002\)032j3145:IVMNTH;2.0.CO;2](https://doi.org/10.1175/1520-0485(2002)032j3145:IVMNTH;2.0.CO;2)
- Crawford, W. R., & Thomson, R. E. (1984). Diurnal-Period Continental Shelf Waves along Vancouver Island: A Comparison of Observations with Theoretical Models. *Journal of Physical Oceanography*, 14(10), 1629–1646. [https://doi.org/10.1175/1520-0485\(1984\)014j1629:dpcswa;2.0.co;2](https://doi.org/10.1175/1520-0485(1984)014j1629:dpcswa;2.0.co;2)
- Cummins, P. F., Masson, D., & Foreman, M. G. G. (2000). Stratification and mean flow effects on diurnal tidal currents off Vancouver Island. *Journal of Physical Oceanography*, 30(1), 15–30. [https://doi.org/10.1175/1520-0485\(2000\)030j0015:SAMFEO;2.0.CO;2](https://doi.org/10.1175/1520-0485(2000)030j0015:SAMFEO;2.0.CO;2)
- D'Asaro, E. A. (1985). The energy flux from the wind to near-inertial motions in the surface mixed layer. *J. Phys. Oceanogr.*, 15(8, Aug. 1985), 1043–1059. [https://doi.org/10.1175/1520-0485\(1985\)015j1043:tefftw;2.0.co;2](https://doi.org/10.1175/1520-0485(1985)015j1043:tefftw;2.0.co;2)
- Drakopoulos, P. G., & Marsden, R. F. (1993). The internal tide off the west coast of Vancouver Island. *Journal of Physical Oceanography*, 23(4), 758–775. [https://doi.org/10.1175/1520-0485\(1993\)023j0758:TITOTW;2.0.CO;2](https://doi.org/10.1175/1520-0485(1993)023j0758:TITOTW;2.0.CO;2)
- Garratt, J. R. (1977). Review of Drag Coefficients over Oceans and Continents. [https://doi.org/10.1175/1520-0493\(1977\)1052.0.CO;2](https://doi.org/10.1175/1520-0493(1977)1052.0.CO;2)

- Garrett, C., & Munk, W. (1979). internal waves in the Ocean. In *Ann. Rev. Fluid Mech* (Vol. 11).
- Gemmrich, J., & Klymak, J. M. (2015). Dissipation of internal wave energy generated on a critical slope. *Journal of Physical Oceanography*, 45(9), 2221–2238. <https://doi.org/10.1175/JPO-D-14-0236.1>
- Gonella, J. (1972). A rotary-component method for analysing meteorological and oceanographic vector time series (Vol. 19). Pergamon Press.
- Hendershott, M. C., & Garrett, C. (2018). Internal Tides. In *Geophysical Fluid Dynamics* (No. 6). Retrieved from <https://gfd.whoi.edu/wp-content/uploads/sites/18/2018/03/lecture0621>
- Hotchkiss, F. S., & Wunsch, C. (1982). Internal waves in Hudson Canyon with possible geological implications. *Deep Sea Research Part A, Oceanographic Research Papers*, 29(4), 415–442. [https://doi.org/10.1016/0198-0149\(82\)90068-1](https://doi.org/10.1016/0198-0149(82)90068-1)
- Johnston, T. M. S., & Rudnick, D. L. (2015). Trapped diurnal internal tides, propagating semidiurnal internal tides, and mixing estimates in the California Current System from sustained glider observations, 2006–2012. *Deep-Sea Research Part II: Topical Studies in Oceanography*, 112, 61–78. <https://doi.org/10.1016/j.dsr2.2014.03.009>
- Klymak, J. M., Alford, M. H., Pinkel, R., Lien, R. C., Yang, Y. J., & Tang, T. Y. (2011). The breaking and scattering of the internal tide on a continental slope. *Journal of Physical Oceanography*, 41(5), 926–945. <https://doi.org/10.1175/2010JPO4500.1>
- Kundu, P. K., & Cohen, I. (2008). *Fluid mechanics*. (4th ed.). Academic Press.
- Kunze, E. (2017). Internal-wave-driven mixing: Global geography and budgets. *Journal of Physical Oceanography*, 47(6), 1325–1345. <https://doi.org/10.1175/JPO-D-16-0141.1>
- Kunze, E., Rosenfeld, L. K., Carter, G. S., & Gregg, M. C. (2002). Internal waves in Monterey Submarine Canyon. *Journal of Physical Oceanography*, 32(6), 1890–1913. [https://doi.org/10.1175/1520-0485\(2002\)032;1890:internal waveIMSC;2.0.CO;2](https://doi.org/10.1175/1520-0485(2002)032;1890:internal waveIMSC;2.0.CO;2)
- Kunze, E., Mackay, C., Mcphee-Shaw, E. E., Morrice, K., Girton, J. B., & Terker, S. R. (2012). Turbulent mixing and exchange with interior waters on sloping boundaries. *Journal of Physical Oceanography*, 42(6),

- 910–927. <https://doi.org/10.1175/JPO-D-11-075.1>
- Kuroda, H., Kusaka, A., Isoda, Y., Honda, S., Ito, S., & OniTuka, T. (2018). Diurnal tidal currents attributed to free baroclinic coastal-trapped waves on the Pacific shelf off the southeastern coast of Hokkaido, Japan. *Continental Shelf Research*, 158, 45–56. <https://doi.org/10.1016/j.csr.2018.02.010>
- Lamb, K. G. (2014). Internal wave breaking and dissipation mechanisms on the continental slope/shelf. *Annual Review of Fluid Mechanics*, 46, 231–254. <https://doi.org/10.1146/annurev-fluid-011212-140701>
- Levine, M. D. (2002). A modification of the Garrett-Munk internal wave spectrum. *Journal of Physical Oceanography*, 32(11), 3166–3181. [https://doi.org/10.1175/1520-0485\(2002\)032j3166:AMOTGMj2.0.CO;2](https://doi.org/10.1175/1520-0485(2002)032j3166:AMOTGMj2.0.CO;2)
- Li, M., Myers, P. G., & Freeland, H. (2005). An examination of historical mixed layer depths along Line P in the Gulf of Alaska. *Geophysical Research Letters*, 32(5), 1–4. <https://doi.org/10.1029/2004GL021911>
- Marques, O. B., Alford, M. H., Pinkel, R., MacKinnon, J. A., Klymak, J. M., Nash, J. D., ... Braznikov, D. (2020). Internal Tide Structure and Temporal Variability on the Reflective Continental Slope of South-eastern Tasmania. *Journal of Physical Oceanography*, 51(2), 611–631. <https://doi.org/10.1175/jpo-d-20-0044.1>
- Martini, K. I., Alford, M. H., Kunze, E., Kelly, S. M., & Nash, J. D. (2013). Internal bores and breaking internal tides on the Oregon continental slope. *Journal of Physical Oceanography*, 43(1), 120–139. <https://doi.org/10.1175/JPO-D-12-030.1>
- Mihaly, S. F., Thomson, R. E., & Rabinovich, A. B. (1998). Evidence for non-linear interaction between internal waves of inertial and semidiurnal frequency. *Geophysical Research Letters*, 25(8), 1205–1208. <https://doi.org/10.1029/98GL00722>
- Munk, W., & Garrett, C. (1979). Internal Waves and Small-Scale Processes. In C. Wunsch (Ed.), *Evolution of Physical Oceanography*.
- Nash, J. D., Kunze, E., Toole, J. M., & Schmitt, R. W. (2004). Internal tide reflection and turbulent mixing on the continental slope. In *Journal of Physical Oceanography* (Vol. 34). [https://doi.org/10.1175/1520-0485\(2004\)034j1117:ITRATMj2.0.CO;2](https://doi.org/10.1175/1520-0485(2004)034j1117:ITRATMj2.0.CO;2)

- Polzin, K. L., & Lvov, Y. V. (2011). Toward regional characterizations of the oceanic internal wavefield. *Reviews of Geophysics*, 49(4), 4003. <https://doi.org/10.1029/2010RG000329>
- Robertson, R., Dong, J., & Hartlipp, P. (2017). Diurnal Critical Latitude and the Latitude Dependence of Internal Tides, Internal Waves, and Mixing Based on Barcoo Seamount. *Journal of Geophysical Research: Oceans*, 122(10), 7838–7866. <https://doi.org/10.1002/2016JC012591>
- Subeesh, M. P., Unnikrishnan, A. S., & Francis, P. A. (2021). Generation, propagation and dissipation of internal tides on the continental shelf and slope off the west coast of India. *Continental Shelf Research*, 214. <https://doi.org/10.1016/j.csr.2020.104321>
- Terker, S. R., Girton, J. B., Kunze, E., Klymak, J. M., & Pinkel, R. (2014). Observations of the internal tide on the California continental margin near Monterey Bay. *Continental Shelf Research*, 82, 60–71. <https://doi.org/10.1016/j.csr.2014.01.017>
- Thomson, R. E., & Crawford, W. R. (1982). The Generation of Diurnal Period Shelf Waves by Tidal Currents in: *Journal of Physical Oceanography* Volume 12 Issue 7 (1982). *Journal of Physical Oceanography*, 12(7).
- Thomson, R. E., Roth, S. E., & Dymond, J. (1990). Near-inertial motions over a mid-ocean ridge: Effects of topography and hydrothermal plumes. *Journal of Geophysical Research*, 95(C5), 7261. <https://doi.org/10.1029/jc095ic05p07261>
- Thomson, R. E., & Fine, I. V. (2003). Estimating mixed layer depth from oceanic profile data. *Journal of Atmospheric and Oceanic Technology*, 20(2), 319–329. [https://doi.org/10.1175/1520-0426\(2003\)020;0319:EMLDFO;2.0.CO;2](https://doi.org/10.1175/1520-0426(2003)020;0319:EMLDFO;2.0.CO;2)
- Thomson, R. E., & Emery, W. J. (2014). Data Analysis Methods in Physical Oceanography: Third Edition. In *Data Analysis Methods in Physical Oceanography: Third Edition (Third)*. <https://doi.org/10.1016/C2010-0-66362-0>
- Thomson, R. E., & Krassovski, M. V. (2015). Remote alongshore winds drive variability of the California Undercurrent off the British Columbia-Washington coast. *Journal of Geophysical Research: Oceans*, 120(12), 8151–8176. <https://doi.org/10.1002/2015JC011306>
- Voelker, G. S., Olbers, D., Walter, M., Mertens, C., & Myers, P. G. (2020). Estimates of wind power and radiative near-inertial internal wave flux: The

- hybrid slab model and IT application to the North Atlantic. *Ocean Dynamics*, 70(11), 1357–1376. <https://doi.org/10.1007/s10236-020-01388-y>
- Xie, X., & Chen, D. (2021). Near-surface reflection and nonlinear effects of low-mode internal tides on a continental slope. *Journal of Physical Oceanography*, 51(4), 1037–1051. <https://doi.org/10.1175/JPO-D-20-0197.1>
- Xie, X., Liu, Q., Zhao, Z., Shang, X., Cai, S., Wang, D., & Chen, D. (2018). Deep Sea Currents Driven by Breaking Internal Tides on the Continental Slope. *Geophysical Research Letters*, 45(12), 6160–6166. <https://doi.org/10.1029/2018GL078372>
- Zheng, J., Tian, J., & Liang, H. (2017). Observation of near-inertial internal waves on the continental slope in the northwestern South China Sea. *Journal of Ocean University of China*, 16(2), 184–190. <https://doi.org/10.1007/s11802-017-3153-7>